

# Evidence of Wind Signatures in the Gas Velocity Profiles of Red Geysers

Namrata Roy<sup>1</sup>, Kevin Bundy<sup>1,2</sup>, Rebecca Nevin<sup>3</sup>, Francesco Belfiore<sup>4</sup>, Renbin Yan<sup>5</sup>, Stephanie Campbell<sup>6</sup>, Rogemar A. Riffel<sup>7,8</sup>, Rogerio Riffel<sup>8,9</sup>, Matthew Bershady<sup>10,11,12</sup>, Kyle Westfall<sup>2</sup>, Niv Drory<sup>13</sup>, and Kai Zhang<sup>14</sup> Department of Astronomy and Astrophysics, University of California, 1156 High Street, Santa Cruz, CA 95064, USA; naroy@ucsc.edu <sup>2</sup> UCO/Lick Observatory, Department of Astronomy and Astrophysics, University of California, 1156 High Street, Santa Cruz, CA 95064, USA Center For Astrophysics, Harvard & Smithsonian, 60 Garden Street, Cambridge, MA 02138, USA INAF-Osservatorio Astrofisico di Arcetri, Largo E. Fermi 5, I-50157, Firenze, Italy <sup>5</sup> Department of Physics and Astronomy, University of Kentucky, 505 Rose Street, Lexington, KY 40506-0055, USA School of Physics and Astronomy, University of St Andrews, North Haugh, St Andrews, Fife KY16 9SS, UK Departamento de Física, CCNE, Universidade Federal de Santa Maria, 97105-900, Santa Maria, RS, Brazil <sup>8</sup> Laboratório Interinstitucional de e-Astronomia—LIneA, Rua Gal. José Cristino 77, Rio de Janeiro, RJ-20921-400, Brazil Departamento de Astronomia, Instituto de Física, Universidade Federal do Rio Grande do Sul, CP 15051, 91501-970, Porto Alegre, RS, Brazil

University of Wisconsin-Madison, Department of Astronomy, 475 North Charter Street, Madison, WI 53706-1582, USA

11 South A frican Astronomical Observatory, P.O. Roy 9 Observatory, 7035, Cane Town, South Africa South African Astronomical Observatory, P.O. Box 9, Observatory 7935, Cape Town, South Africa <sup>12</sup> Department of Astronomy, University of Cape Town, Private Bag X3, Rondebosch 7701, South Africa 13 McDonald Observatory, The University of Texas at Austin, 2515 Speedway, Stop C1402, Austin, TX 78712, USA Lawrence Berkeley National Laboratory, 1 Cyclotron Road, Berkeley, CA 94720, USA Received 2020 December 17; revised 2021 March 12; accepted 2021 March 23; published 2021 May 21

#### **Abstract**

Spatially resolved spectroscopy from the Sloan Digital Sky Survey IV Mapping Nearby Galaxies at Apache Point Observatory (MaNGA) survey has revealed a class of quiescent, relatively common early-type galaxies termed "red geysers" that possibly host large-scale active galactic nuclei—driven winds. Given their potential importance in maintaining a low level of star formation at late times, additional evidence confirming that winds are responsible for the red geyser phenomenon is critical. In this work, we present follow-up observations with the Echellette Spectrograph and Imager (ESI) at the Keck telescope of two red geysers (z < 0.1) using multiple long slit positions to sample different regions of each galaxy. Our ESI data with a spectral resolution (R) ~ 8000 improve upon MaNGA's resolution by a factor of 4, allowing us to resolve the ionized gas velocity profiles along the putative wind cone with an instrumental resolution of  $\sigma = 16 \, \mathrm{km \, s}^{-1}$ . The line profiles of  $H\alpha$  and [N II]  $\lambda$ 6584 show asymmetric shapes that depend systematically on location: extended blue wings on the redshifted side of the galaxy and red wings on the opposite side. We construct a simple wind model and show that our results are consistent with geometric projections through an outflowing conical wind oriented at an angle toward the line of sight. An alternative hypothesis that assigns the asymmetric pattern to "beam smearing" of a rotating, ionized gas disk does a poor job matching the line asymmetry profiles. While our study features just two sources, it lends further support to the notion that red geysers are the result of galaxy-scale winds.

*Unified Astronomy Thesaurus concepts*: AGN host galaxies (2017); Early-type galaxies (429); Elliptical galaxies (456); Emission line galaxies (459); Galaxies (573); LINER galaxies (925); Quenched galaxies (2016); Galactic winds (572)

#### 1. Introduction

"Maintenance" or "radio" mode feedback resulting from low-to-moderate-luminosity active galactic nuclei (AGNs) has been proposed as a means for maintaining low levels of star formation (log SFR <  $-2 M_{\odot} \text{yr}^{-1}$ ) at late times, thereby explaining the massive increase in the number of red galaxies since  $z \sim 2$  (Bell et al. 2004; Bundy et al. 2006; Croton et al. 2006; Faber et al. 2007; Ilbert et al. 2010; Moustakas et al. 2013). These radio AGNs are thought to be radiatively inefficient, accreting at low rates and depositing most of their energy to their surroundings via momentum-driven winds or radio jets (Binney & Tabor 1995; Ciotti & Ostriker 2001; Bower et al. 2006; Croton et al. 2006; Ciotti & Ostriker 2007; McNamara & Nulsen 2007; Cattaneo et al. 2009; Ciotti et al. 2010; Fabian 2012; Heckman & Best 2014; Yuan & Narayan 2014). This input energy heats ambient gas that might otherwise cool and form stars, thus maintaining quenched galaxies in a passive state. Although evidence for radio-mode AGN feedback has been observed in the form of large bubbles of ionized gas and radio jets in the centers of massive clusters and giant radio galaxies (Fabian 1994, 2012;

Dunn & Fabian 2006; Fabian et al. 2006; McNamara & Nulsen 2007; Cattaneo et al. 2009), it has been difficult to find evidence for this mechanism operating in lower-mass halos that host typical quiescent galaxies (halo mass  $< 10^{12} M_{\odot}$ ).

We have been studying a population of moderate-mass (log  $M_{\star}/M_{\odot} \sim 10.5$ ) red quiescent galaxies (NUV – r > 5) known as "red geysers" (Cheung et al. 2016; Roy et al. 2018) that may hold clues in this regard. Identified in low-redshift integral field spectroscopy from the Sloan Digital Sky Survey IV (SDSS-IV) Mapping Nearby Galaxies at Apache Point Observatory (MaNGA) survey (Bundy et al. 2015), these galaxies are characterized by bisymmetric equivalent width (EW) maps of strong emission lines like H $\alpha$ , [N II]  $\lambda\lambda6548$ , 84, and [O III]  $\lambda\lambda 4959$ , 5007, which appear to be tracing large-scale ionized gas outflows. This distinctive emission pattern roughly aligns with the gas kinematic axis but is strongly misaligned with the stellar velocity gradient. The gas velocity values reach  $\sim \! \! 300 \; \mathrm{km \, s^{-1}}$  compared to less than  $40 \; \mathrm{km \, s^{-1}}$  in the stars. These galaxies lack star formation with an average log SFR  $[M_{\odot} \text{ yr}] < -2$  (using GALEX+SDSS+WISE; Salim et al. 2016). They additionally show a high value of the 4000Å break

index (D4000) with an average value of >2.0, thus providing further evidence that young stars are absent in the galaxy. Spatially resolved Baldwin–Phillips–Terlevich (BPT) diagrams (Baldwin et al. 1981) indicate widespread ionization with line ratios consistent with a combination of low-ionization nuclear emission region (LINER) and Seyfert values. The morphology of these galaxies is spheroidal with a high Sérsic index ( $n \ge 3$ ).

Although the observed characteristics of the red geysers can be explained by a centrally driven wind, early-type galaxies with accreted gas disks (Sarzi et al. 2006; Davis et al. 2013; Lagos et al. 2014, 2015; Chen et al. 2016; Bryant et al. 2019; Starkenburg et al. 2019; Duckworth et al. 2020) can also show similar kinematic misalignment and emission features due to rotation of the gaseous material in the disk. However, 95% of the red geyser sample are fast-rotator early-type galaxies from the Graham et al. (2018) catalog (Roy et al. 2018), and it is considerably difficult for a gas disk to be in equilibrium if it is misaligned with the stellar kinematic axis because of the axisymmetric nature of the fast rotators (although see van de Voort et al. 2015; Davis & Bureau 2016). The red geysers are also selected to have an axis ratio b/a > 0.4 (Roy et al. 2018) with no visible dust lanes, as seen from SDSS imaging, in order to exclude any edge-on disks in the sample. A disturbed disk with a chaotic accretion scenario is still possible, and further investigation is therefore needed to confirm otherwise.

In Roy et al. (2018), we reported evidence for the presence of faint radio AGNs in the red geyser galaxies. Stacked 1.4 GHz radio flux from the Very Large Array (VLA) Faint Images of the Radio Sky at Twenty-Centimeters (FIRST) survey shows significantly ( $>5\sigma$ ) higher radio flux in red geysers than a matched control sample. Red geysers also show a radio detection rate that is three times higher than the control. Roy et al. (2018) showed that this radio emission indicates lowluminosity radio AGNs ( $L_{1.4~\rm GHz} \sim 10^{22} - 10^{23}~\rm W~Hz^{-1}$ ) with radiatively inefficient accretion (Eddington scaled accretion rate  $\lambda \sim 10^{-4}$ ). Recently, Duckworth et al. (2020) indicated a tentative correlation between enhanced AGN activity and misaligned gas disks in low-mass galaxies (log  $M < 10.2 M_{\odot}$ ) using IllustrisTNG simulations. However, no such trend has been found in a high-mass quenched population having a similar mass as the red geyser sample. Hence, the enhancement in radio AGN activity seen in the red geysers cannot be immediately attributed to the phenomena of misaligned gas disks. Riffel et al. (2019) studied the launching of these proposed winds with Gemini Multi-Object Spectrograph (GMOS) observations of the prototypical red geyser in Cheung et al. (2016) to constrain the gas kinematics in the nuclear region. They observed the emission line flux distributions and gas kinematics within the inner 1" to be distinct and misaligned from that of the outer regions, 5'' away from center, a result that may indicate precession of the accretion disk.

Cheung et al. (2016) presented a variety of evidence, including dynamical modeling and geometric arguments, that lends support for an interpretation of red geysers as an AGN-driven wind phenomenon (see also Gomes et al. 2016). However, it is important to seek out additional lines of evidence to distinguish outflows from rotation. In this work, we examine further evidence for the wind interpretation through follow-up Keck spectroscopy of red geyser galaxies with higher spectral resolution ( $R \sim 8000$ ) than the original MaNGA data ( $R \sim 2000$ ). The improved resolution allows us to search for detailed kinematic signatures of outflowing winds that are

blurred at MaNGA's instrumental resolution. We detect asymmetric emission lines that vary in a systematic manner along the kinematic major axis, which likely indicates the specific geometry of the wind along the line of sight. For the two red geysers (MaNGA ID: 1-217022 and 1-145922) studied here with the Keck Echellette Spectrograph and Imager (ESI) instrument, we find results consistent with our simple wind model. An alternative hypothesis that assigns the asymmetric pattern to the beam smearing of a rotating, ionized gas disk is not favored by our data.

Throughout this paper, we assume a flat cosmological model with  $H_0 = 70$  km s<sup>-1</sup> Mpc<sup>-1</sup>,  $\Omega_m = 0.30$ , and  $\Omega_{\Lambda} = 0.70$ , and all magnitudes are given in the AB magnitude system.

# 2. Observation and Data Acquisition

#### 2.1. The MaNGA Survey

We use observations from the SDSS-IV MaNGA survey (Bundy et al. 2015; Drory et al. 2015; Law et al. 2015; Yan et al. 2016a; Albareti et al. 2017; Blanton et al. 2017). MaNGA is an integral field spectroscopic survey that provides spatially resolved spectroscopy for nearby galaxies ( $z \sim 0.03$ ) with an effective spatial resolution of 2"4 (FWHM). The MaNGA survey uses the SDSS 2.5 m telescope in spectroscopic mode (Gunn et al. 2006) and the two dual-channel BOSS spectrographs (Smee et al. 2013) that provide continuous wavelength coverage from the near-UV to the near-IR: 3600-10000 Å. The spectral resolution varies from  $R \sim 1400$  at 4000 Å to  $R \sim 2600$ at 9000 Å. An r-band signal-to-noise ratio (S/N) of 4–8 Å<sup>-1</sup> is achieved in the outskirts (i.e.,  $1-2R_e$ ) of the target galaxies with an integration time of approximately 3 hr. MaNGA has observed roughly 10,000 galaxies with  $\log (M_*/M_{\odot}) \gtrsim 9$ across  $\sim$ 2700 deg<sup>2</sup> over its 6 yr duration. In order to balance radial coverage versus spatial resolution, MaNGA observes two-thirds of its galaxy sample to  $\sim 1.5 R_e$  and one-third to  $2.5 R_e$ . The MaNGA target selection is described in detail in Wake et al. (2017).

The raw data are processed with the MaNGA Data Reduction Pipeline (DRP; Law et al. 2016; Yan et al. 2016b). An individual row-by-row algorithm is used to extract the fiber flux and derive inverse variance spectra from each exposure, which are then wavelength-calibrated, flat-fielded, and sky-subtracted. We use the MaNGA sample and data products drawn from the MaNGA Product Launch-8 (MPL-8; see Table 1 from Law et al. 2021). We use spectral measurements and other analyses carried out by version 2.3.0 of the MaNGA Data Analysis Pipeline (DAP). The data we use here are based on DAP analysis of each spaxel in the MaNGA data cubes. The final output from the DAP includes gas and stellar kinematics, emission line properties, and stellar absorption indices. All of the spatially resolved 2D maps shown in the paper are outputs from the DAP. An overview of the DAP used for Data Release 15 (DR15) and its products is described by Westfall et al. (2019), and assessments of its emission line fitting approach are described by Belfiore et al. (2019).

We use ancillary data drawn from the NASA Sloan Atlas<sup>15</sup> (NSA) catalog, which reanalyzes images and derives morphological parameters for local galaxies observed in SDSS imaging (Blanton et al. 2011). It compiles spectroscopic redshifts, UV

<sup>15</sup> http://www.nsatlas.org

photometry (from GALEX; Martin et al. 2005), stellar masses (Blanton & Roweis 2007), and structural parameters.

#### 2.2. Keck ESI Data

The ESI is a visible-wavelength, faint-object imager and single-slit spectrograph that has been in operation at the Cassegrain focus of the Keck II telescope since 1999. The ESI has three modes of observation: echellette mode, low dispersion mode, and direct imaging mode. The mode of operation used here is the echellette mode, which provides a cross-dispersed spectroscopy mode at a resolving power of up to R = 13,000. Slits are 20" in length and available with widths of 0."3, 0."5, 0."75, 1."0, 1."25, and 6."0 with varying spatial scales and velocity resolution. The echellette mode disperses the light into 10 orders with a dispersion ranging from  $\sim 0.30 \,\text{Åpixel}^{-1}$  in order six (red) to  $\sim 0.16 \,\text{Åpixel}^{-1}$  in order 15 (blue), while maintaining a roughly constant dispersion of 11.5 km s<sup>-1</sup> pixel<sup>-1</sup> in velocity across all orders. The orders are curved due to the distortion within the prisms. The ESI has a wide spectral coverage spanning from 0.39 to  $1.1~\mu m$  in a single exposure and a velocity resolution as low as 22 km s<sup>-1</sup> FWHM (using the 0",3 wide echellette slit). An Epps refracting camera and a single 2K × 4K detector are used for all three modes.

Utilizing two half-nights in 2017 February, we followed up two red geysers from our MaNGA sample. These targets completely fill the ESI's 20" slit. We were able to observe both targets with multiple slit positions to map out different parts of the galaxy. For the first target galaxy, ID 1-217022, which is the prototypical red geyser "Akira" from Cheung et al. (2016), we observed three slit positions, while for the second target (ID 1-145922), we observed two slit positions. For each slit position, we integrated for 1.5-2 hr (in source and sky combined), nodding to sky positions every 5 minutes to enable quality sky subtraction. However, for the second slit for the second target, a combination of high clouds and a lower integration time resulted in unacceptably low-S/N spectra. Hence, we discarded that slit for our present analyses. We took measurements of the standard star G191b2b at the beginning of each night with the same instrumental setting with an exposure of 3 minutes to perform flux calibration. The width of the slit for all observations was 0."5, yielding a velocity resolution of  $\sim$ 37 km s<sup>-1</sup> or  $R \sim$ 8000. The median seeing FWHM over the course of the observations was 0."9. This should be compared to MaNGA's  $R \sim 2000$  spectral resolution and its effective spatial resolution of 2"4.

Figures 1 and 2 show the slit positions for the two galaxies, respectively, overlaid on their optical image (left panel) and their MaNGA ionized gas velocity fields with  $H\alpha$  EW contours on top (right panel). In the first target, slit 1 was placed at an angle of 40° from north to east, tracing the bisymmetric emission feature. Slit 2 was placed at an angle of 110° from north to east to sample the central parts of the galaxy and intersect with slit 1 at the center. Slit 3 ran parallel to slit 1 at an offset of  $\sim 4.9$  in the southeast direction. In the second galaxy, the slit was placed at an angle of 320° from north to east along its biconical pattern.

We used routines from the *ESIRedux* package, developed by Jason X. Prochaska to aid in reducing the ESI data. This package was primarily built in IDL and is publicly available.<sup>16</sup>

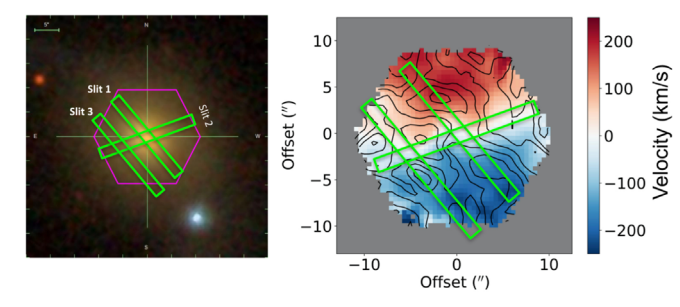


**Figure 1.** Keck ESI slit positions for the first target galaxy (MaNGA ID: 1-217022). The left and right panels show the three slit positions overlaid on the SDSS optical image and the MaNGA ionized gas velocity map, respectively. The black contours in the velocity map show the  $H\alpha$  EW. Slit 1, placed at an angle of  $40^\circ$  from north to east, traces the bisymmetric emission feature. Slit 2 is placed at an angle of  $110^\circ$  from north to east, sampling the central parts of the galaxy. Slit 3 is placed parallel to slit 1 with an offset of  $\sim 4\rlap/\!'/9$ .

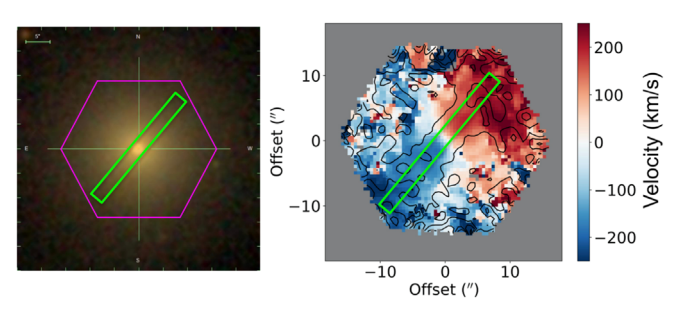


**Figure 2.** The ESI slit positions for the second target (MaNGA ID: 1-145922). The left and right panels show the slit position on the optical image and the MaNGA gas velocity map, respectively. The black contours in the velocity map show the H $\alpha$  EW. The slit is placed at an angle of 320° from north to east, tracing the biconical emission feature.

Our primary goal is to extract spatially resolved spectra along the multiple slits of our targets, whose angular extent on the sky fills the slit ( $\sim 20''$ ). This requires some steps in addition to the *ESIRedux* pipeline. The detailed description of the data reduction steps is given in the next section.

# 2.3. ESI Data Reduction

We begin by using *ESIRedux* to perform bias subtraction, flat-field correction, and wavelength calibration. Several dome flats are taken at the beginning of each night with the same instrument setup as the target observations. In the first step, the routine identifies and combines the bias and flat frames separately to create a median bias and a median flat frame. The median bias is subtracted from the image. The bias-subtracted image is then normalized by the median flat. The resulting image is then run through the wavelength calibration routine in the pipeline.

We utilize Python routines to do the rest of the reduction steps. Since all of the targets fill the 20" ESI slit, object detection and sky spectra extraction cannot be performed with ESIRedux routines. Separate sky observations were taken near the target during observations roughly 50% of the time, alternatively switching between the sky and the targets. Sky subtraction is done by directly subtracting the sky image from the science image taken closest in time. We also account for small telescope pointing offsets that may arise between different exposures by cross-correlating and shifting the spectra from different exposure frames with respect to each other in

<sup>16</sup> https://www2.keck.hawaii.edu/inst/esi/ESIRedux/

order to be aligned perfectly. A  $3\sigma$  clipping routine is then applied to the sky-subtracted science images to remove cosmic rays. Finally, the individual exposures are added together to form a combined 2D image. Using the 2D wavelength solution obtained from wavelength calibration and the coadded 2D science image, we extract 1D spectra from each spatial pixel along the slit for each individual echellette order. Finally, we stitch all 10 echellette orders together to form a continuous spectrum over the entire wavelength range. To improve the S/N and ensure a minimum S/N > 1 over the entire extent of the slit, the spectra are binned spatially with a bin size of 1".

The final step of the data reduction is flux calibration. Standard-star (G191b2b) observations taken at the beginning of each night have been used to calibrate the spectra to first order. Flux calibration initially corrects for two effects: the blaze effect caused by the instrument response of the echelle grating and the conversion from photon counts to flux density in physical units. Both effects are corrected using standard-star observations by comparing the absolute flux of the standard star to the observed counts sampled at the same wavelength. However, the science spectra, which have been flux-calibrated in this manner, show a systematic difference in flux values with that of the MaNGA spectra by a nonnegligible amount. The possible reason behind this mismatch maybe inaccurate blaze function removal, nonphotometric conditions or variations along the slit. Since we already possess MaNGA spectra for our targets with a flux calibration accuracy to a few percent (Yan et al. 2016a), we use the MaNGA spectra as a reference to correct for residual inaccuracies in the flux-calibrated Keck spectra.

To perform this second step of flux calibration, we obtain the sky positions of each of the 1" Keck ESI spatial bins (hereafter spaxels) on the target galaxy. We then find the MaNGA spaxels that overlap in sky position, yielding 1-1 spatial mapping between the MaNGA spaxels (of size  $\sim 0.75$ ) and ESI binned spaxels (1"). Next, for each ESI spaxel, we take the corresponding MaNGA spectrum (from the spatial mapping) and smooth it using a Gaussian filter. The smoothing uses a fairly large spectral window size while disregarding emission lines and other sharp spectral features. The smoothed MaNGA spectrum is then fit with a Chebyshev polynomial, the fit being given by the calibration vector,  $P_{\text{MaNGA}}$ . On the other hand, the corresponding ESI spectra is also smoothed by a Gaussian filter but using a window size almost three times as large, owing to the higher spectral resolution. The smoothed ESI spectrum is fit similarly with a Chebyshev polynomial that gives  $P_{\rm ESI}$ . The final corrected flux-calibrated ESI spectrum (ESI<sub>final</sub>) is then obtained by scaling the original ESI spectrum (ESI<sub>original</sub>) by the formula

$$\mathrm{ESI}_{\mathrm{final}} = \mathrm{ESI}_{\mathrm{original}} \frac{P_{\mathrm{MaNGA}}}{P_{\mathrm{ESI}}}.$$

The above process is repeated for all spectra along each ESI slit. An example of a reduced ESI spectrum is shown in Figure 3.

# 3. Method and Analysis

#### 3.1. Sample Selection

Our parent sample of red geysers consists of 84 galaxies that account for  $\approx 8\%$  of the quiescent MaNGA population (Roy et al. 2018). The red geyser sample is visually selected based on the following characteristic features.

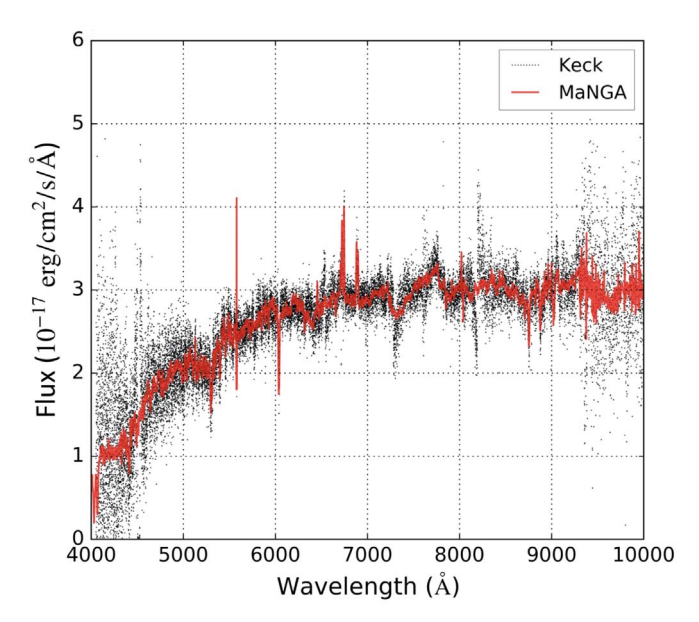


**Figure 3.** Example of a reduced Keck ESI spectrum (in black) in a 1" spatial bin along the ESI slit. MaNGA spectra from the spaxel corresponding to the same physical position on the sky are overplotted in red.

- 1. Very low star formation rate with a typical value of log SFR  $[M_{\odot} \text{ yr}^{-1}] \sim -3$ , measured by optical–IR SED fitting (Chang et al. 2015; Salim et al. 2016), and rest-frame color NUV -r > 5.
- 2. Bisymmetric emission feature in spatially resolved  ${\rm H}\alpha$  EW 2D map.
- 3. Rough alignment of the bisymmetric feature with the ionized gas kinematic axis but misalignment with the stellar kinematic axis.
- 4. High spatially resolved gas velocity values, typically reaching a maximum of 300 km s<sup>-1</sup>, which are greater than the stellar velocity values by a few factors.

Further details about the full sample are given in Roy et al. (2018).

The two red geyser candidates selected for the Keck ESI follow-up represent a range of different values of H $\alpha$  flux, EW, ionized gas velocity, misalignment angle, and radio flux while having sky positions amenable to the allocated Keck observing time. Hence, they are good representations of the entire parent sample. The two chosen targets are shown in Figures 4 and 5. The first galaxy (ID: 1-217022) is the prototypical red geyser (Cheung et al. 2016), which shows all of the characteristics mentioned above and is among the first ones discovered in MaNGA. Its relevant characteristics are highlighted in Figure 4. The top left panel in the figure shows the H $\alpha$  flux distribution, which is extended in nature and shows a high value compared to other passive quenched galaxies, surpassing  $\sim 5 \times 10^{-16} \, \mathrm{erg \, cm^{-2} \, s^{-1}}$ . The galaxy has a clear bisymmetric pattern in the H $\alpha$  EW map with an average EW  $\sim$ 4.5 Å (bottom left panel). The top and bottom middle panels show the stellar and gas velocity maps, respectively. Cheung et al. (2016) performed detailed dynamical modeling of the gas and stellar kinematics in this galaxy to conclude that a centrally driven outflow is the likely explanation for the high  $(\sim 300 \,\mathrm{km \, s^{-1}})$  gas velocity values. The spatially resolved BPT diagrams (right panels) show LINER-like line ratios throughout the galaxy. This galaxy has a central radio source detected in FIRST and Jansky Very Large Array (JVLA)

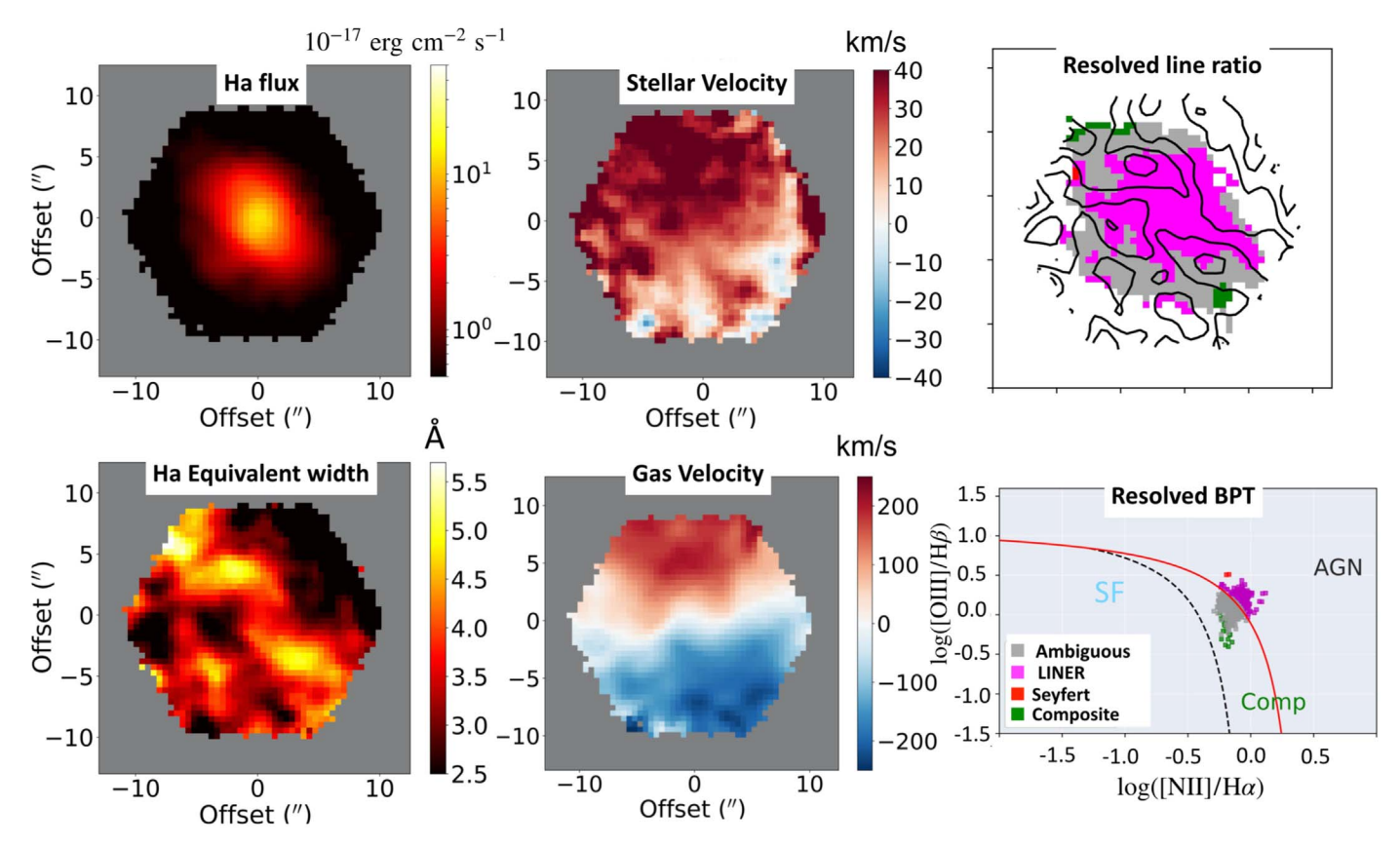


Figure 4. Spatially resolved emission line and kinematic properties of the first target red geyser galaxy from SDSS-IV MaNGA (MaNGA ID: 1-217022). The on-sky diameter of this particular IFU fiber bundle is 22'', which corresponds to a physical size of 11 kpc. The top left panel shows the spatial distribution of  $H\alpha$  flux. In the other panels, as labeled, we show the  $H\alpha$  EW map (bottom left), the 2D stellar velocity field (top middle), and the ionized gas velocity traced by  $H\alpha$  (bottom middle). The bottom right panel shows the spatially resolved BPT diagram showing spaxels with S/N > 3. The top right panel shows the spatial position of those spaxels colored by their classification based on the BPT diagram. Characteristic red geyser features such as the bisymmetric emission feature in  $H\alpha$  and its alignment with the gas kinematics axis are particularly apparent.

1.4 GHz continuum emission (Cheung et al. 2016), which indicates a low-luminosity radio AGN with a low Eddington ratio ( $\lambda \sim 10^{-4}$ ). The presence of ionized gas is evident in the strong detection of Balmer lines and forbidden emission lines like H $\alpha$ , [N II], and [O III].

The second red geyser target (ID: 1-145922) also shows a clear bisymmetric EW pattern (Figure 5) but with a much lower H\$\alpha\$ EW value of \$\sim 1-2.5\$ Å (bottom left panel). LINER-like line ratios are observed throughout most of the galaxy, while AGN/Seyfert line ratios appear in the center (right panels), with  $\log([[N\ II]]/H\alpha) > -0.4$ . Unlike the first target, this galaxy does not show systematic rotation in the stellar kinematics (top middle panel); hence, the exact misalignment angle between the gas and stellar velocity field is unclear. However, the estimated average second velocity moment ( $V_{\rm rms} \equiv \sqrt{V^2 + \sigma^2}$ ) of the ionized gas and stars is similar to the first target. This galaxy is not radio-detected in the FIRST survey and has not been followed up with the JVLA. Both galaxies have spheroidal morphology, as observed from SDSS ground-based imaging.

### 3.2. Line Profile Fitting

An important aspect of accurately measuring emission lines is properly accounting for the stellar continuum. This is particularly important for the Balmer lines, since underlying stellar absorption can lead to incorrect emission line flux and EW estimation. We apply MaNGA's DAP, version 2.3.0

(Westfall et al. 2019), on the fully reduced Keck data for accurate modeling of the stellar continuum throughout the galaxy. First, we run DAP modules on each spaxel in the MaNGA data cube of the target galaxy. The DAP masks  $\pm 750\,\mathrm{km\,s^{-1}}$  surrounding each of the expected emission line regions at the galaxy systemic redshift and fits the stellar continuum using the penalized pixel fitting algorithm pPXF (Cappellari & Emsellem 2004; Cappellari 2017). It uses a combination of 49 templates based on the MILES stellar library, known as the MILES-HC library (Falcón-Barroso et al. 2011), which provides statistically equivalent fits to those that use the full library of 985 spectra in the MILES stellar library (Westfall et al. 2019). Once the DAP fits the continuum and obtains the optimal stellar template for a particular MaNGA spaxel, we use that same template to fit the continuum of the Keck spectra for the corresponding Keck spaxel, again using pPXF. The best-fit stellar continuum is then subtracted from the observed spectrum before we analyze the emission lines.

We treat the H $\alpha$  and [N II]  $\lambda 6584$  Å emission lines independently, fitting for their flux, velocity, and dispersion. At first, we model both the H $\alpha$  line and the [N II]  $\lambda 6584$  Å line as single Gaussian profiles. After binning the ESI slit data into spatial bins of size 1", we constrain the velocity within each bin to be within  $\pm 350$  km s $^{-1}$  of the systemic velocity. This is done to prevent the module from fitting spurious peaks. We also require the dispersion to be less than 500 km s $^{-1}$ . In order to sample the entire parameter space and obtain an unbiased

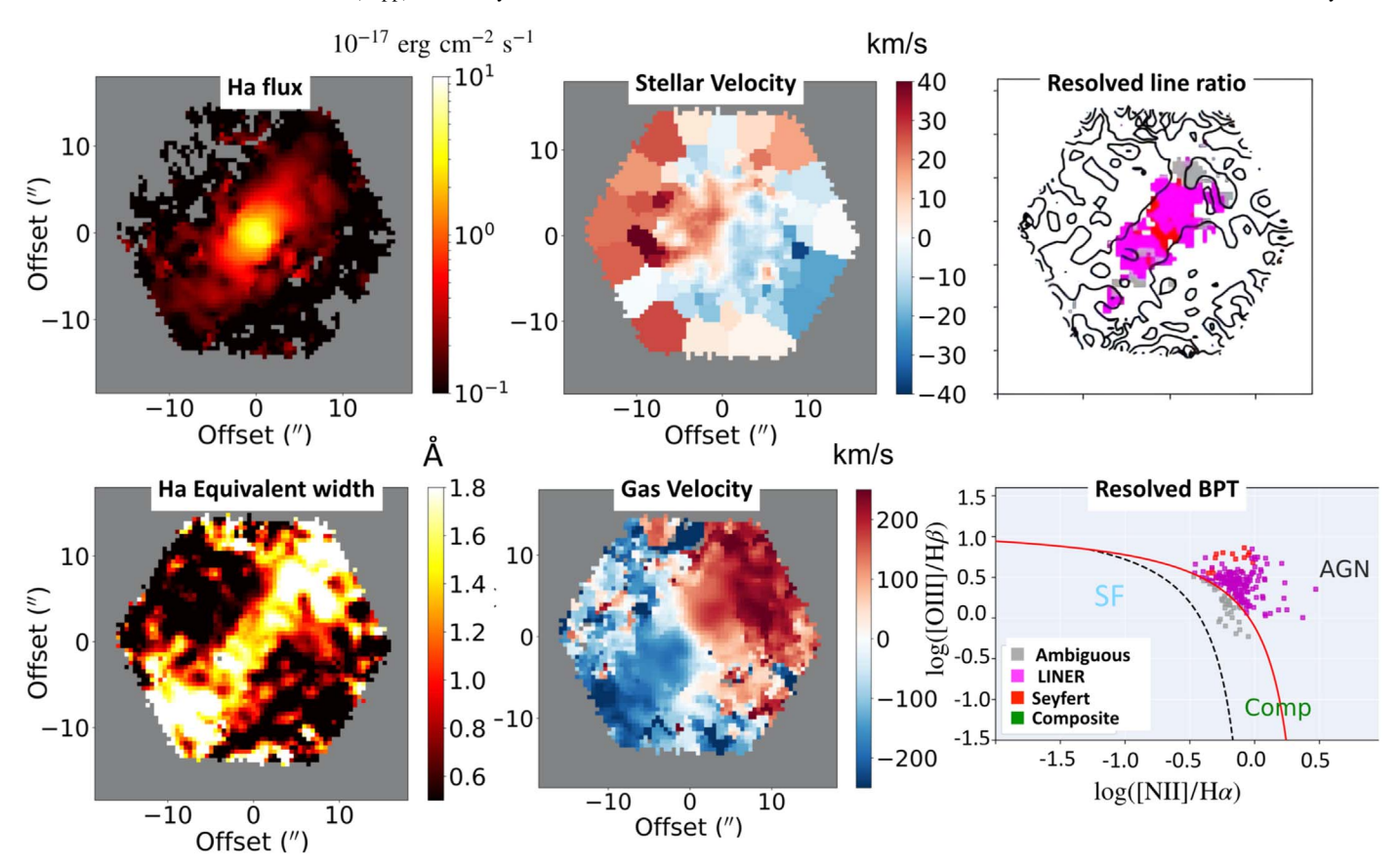


Figure 5. Spatially resolved emission line and kinematic properties of the second target red geyser galaxy from SDSS-IV MaNGA (MaNGA ID: 1-145922). The onsky diameter of this particular IFU fiber bundle is 32", which corresponds to a physical size of 18 kpc. The different panels are the same as in Figure 4.

estimate of the uncertainties in the fitted values, we wrap our fitting procedure in a Markov Chain Monte Carlo (MCMC) framework with a dynamical nested sampling algorithm (Higson et al. 2019) using the Python package *dynesty* (Speagle 2020). The nested sampling method (Skilling 2004, 2006) is used to estimate both the Bayesian evidence and posterior distribution in an iterative fashion until the convergence criteria are met. However, the single Gaussian model results in large residuals for most of the spatial bins (or spaxels). Figure 6(a) shows the single Gaussian fit of the spectrum around the  $H\alpha$ emission line for a particular ESI spaxel in the first target galaxy (MaNGA ID: 1-217022). It is clear from the figure that the emission line shows a large departure ( $\pm 15\%$ ) from the model. We therefore proceed to fit a double Gaussian model to the emission lines, keeping the velocity of the first Gaussian component within  $\pm 50 \,\mathrm{km \, s^{-1}}$  of the velocity estimate obtained from single-component fitting. This "primary component" is constrained to have a greater flux than the "secondary component." The dispersion in the primary component is constrained to be  $<200 \,\mathrm{km \, s^{-1}}$ , while no restriction is imposed on the secondary component. This is done to make sure that the primary component, or the "narrow" component, represents the bulk velocity of the gas, while the secondary component is sensitive to broad wings and other departures from the primary. Figure 6(b) shows the double Gaussian fit of the same spectrum, with the primary component shown in red and the secondary component in green. The resulting fit (blue dashed line) shows that the flux residuals are less than 5% of the median flux.

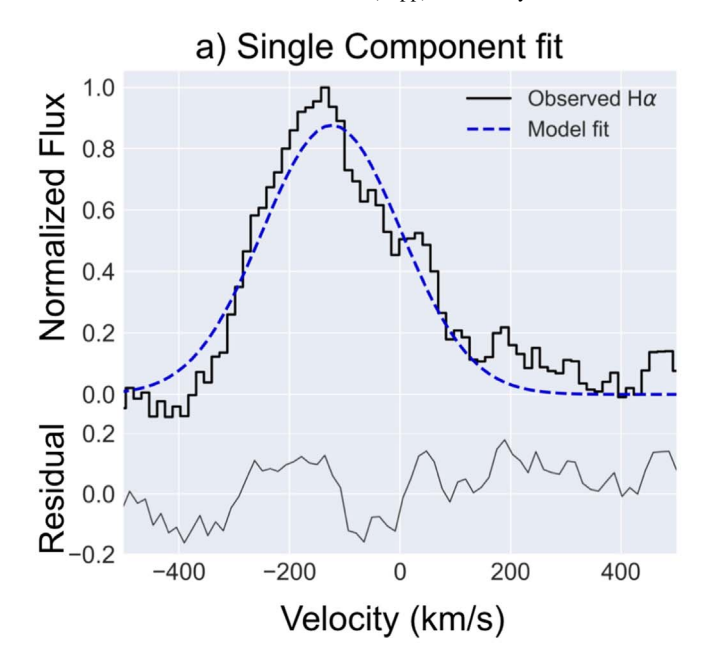
To determine which of the two models is preferred for each spaxel, we use a Bayesian information criterion (BIC), which uses the likelihood to determine the optimum model but penalizes for additional free parameters. It is defined as

$$BIC = -2\mathcal{L} + k \log(N), \tag{1}$$

where  $\mathcal{L}$  is the log-likelihood, k is the number of free parameters, and N is the number of data points that get fit. The model with the lower BIC value is the preferred model, and the final fit is selected accordingly. For example, in Figure 6, the double Gaussian model is preferred over the other.

#### 4. Results

With emission line velocity profiles extracted from the higher-resolution Keck ESI data and fit with a single or double Gaussian model, depending on the BIC criterion, we are ready to investigate systematic patterns in the profile shape emerging in different parts of the galaxy. An example of  $H\alpha$  and [N II] emission line profiles at two opposite ends of the galaxy is shown in Figure 7. This detailed line profile information may inform or refute our earlier wind model interpretation of red geyser gas kinematics that was based on MaNGA data alone. We begin by presenting all of the Ha and [N II] velocity profiles derived from the ESI data at different slit positions for both of the target galaxies.



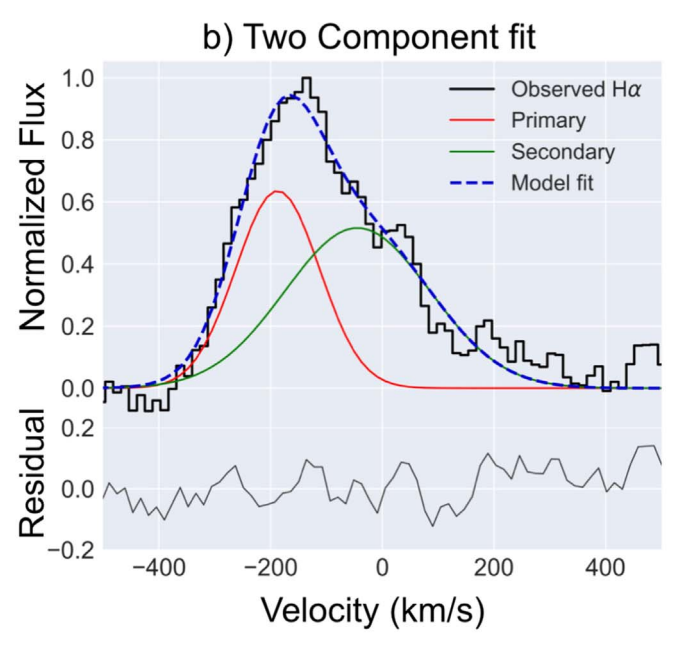


Figure 6. (Top panel) Example of a single Gaussian fit to the continuum-subtracted  ${\rm H}\alpha$  emission line from the ESI at a particular 1" spaxel. The single-component model (shown in blue) leaves a huge residual of about  $\pm 15\%$  as shown in the residual panel. (Bottom panel) A two-component model fit to the same spectrum as above is shown. The model consists of a double Gaussian, with the primary component shown in red measuring the bulk velocity of the gas and the secondary component shown in green showing the wings and departures from the single-component model. This model greatly reduces the residual to only about  $\pm 5\%$  and is favored.

# 4.1. Target 1-217022

For the first target, slit 1 is placed at a position angle of  $40^{\circ}$  from north to east along the bisymmetric emission feature. The observed spectra are shown in Figure 8. The top panel shows the MaNGA 2D ionized gas velocity field of the target, with  $H\alpha$  EW contours overplotted in black. The slit position is overlaid, with white filled circles indicating the different spaxels of 1" where reduced spectra have been extracted. In the bottom panel, the different rows indicate those reduced spectra

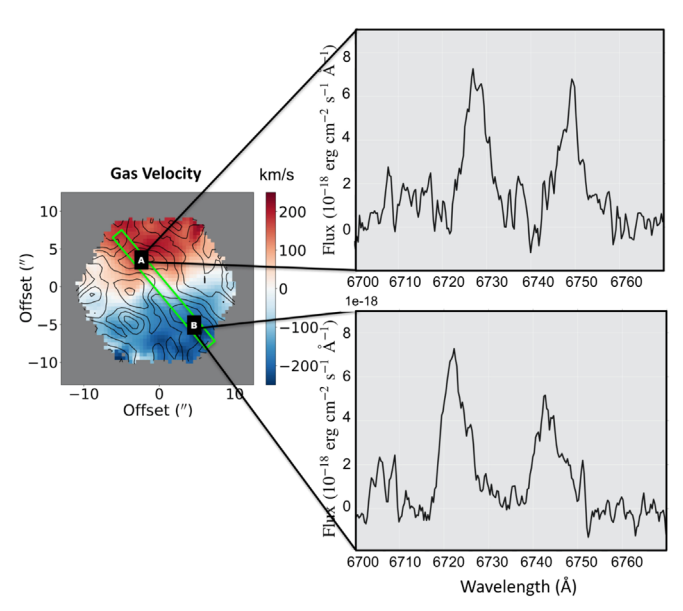


Figure 7. (Left panel) The 2D gas velocity field of the first target galaxy obtained from MaNGA data with  $H\alpha$  EW contours overplotted in black. (Right panel) The  $H\alpha$  and [N II]  $\lambda$ 6584 emission line profiles obtained from the Keck ESI at two separate locations in the galaxy, indicated by A and B in the left panel. The emission line profiles reveal a complex velocity structure likely resulting from multiple components. Extended wings in the emission lines switch from the blue side at position A to the red side at position B.

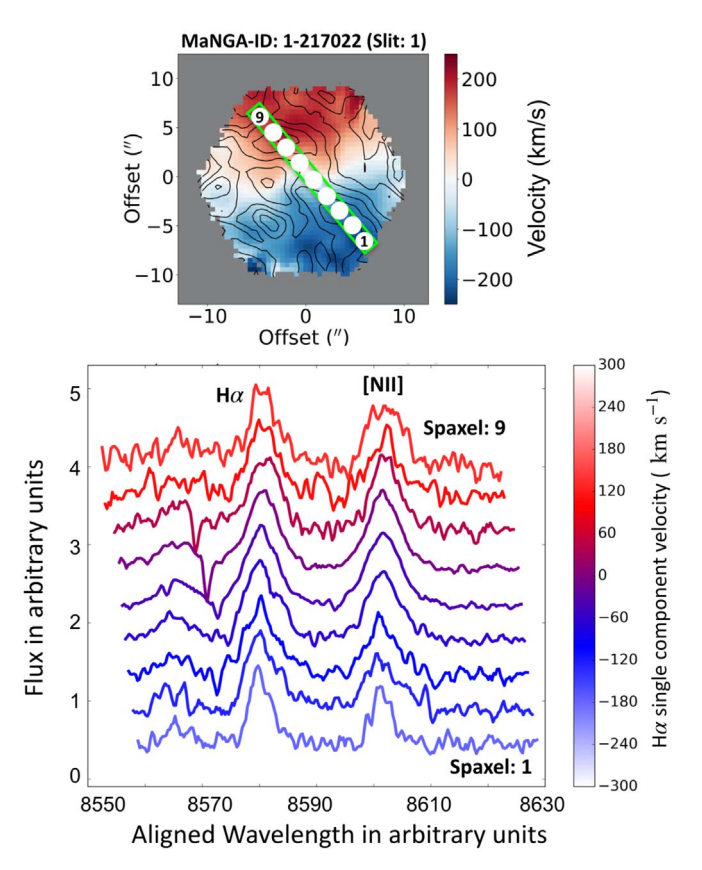


Figure 8. (Top panel) The 2D ionized gas velocity field of the first target galaxy obtained from MaNGA data with the  $H\alpha$  EW contours overplotted in black. The first slit position with different spatial bins ( $\sim$ 1") is overlaid to map the physical location of the extracted spectra on the slit. (Bottom panel) The different rows indicate the observed spectra from the Keck ESI around the spectral window of  $H\alpha$  and [N II]  $\lambda$ 6584 extracted from different spatial bins (or spaxels) as marked in the top panel. The spectra are registered to the same wavelength and color-coded by gas velocity.

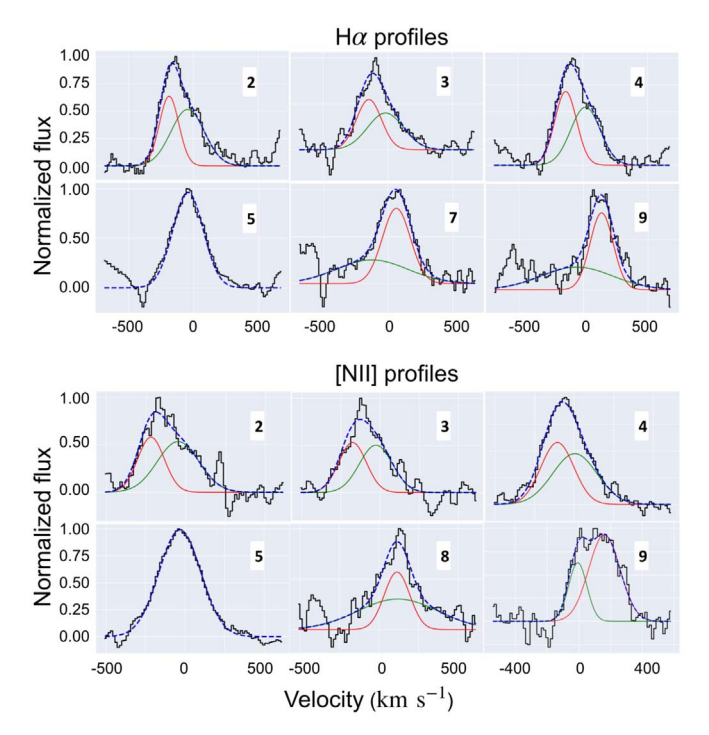
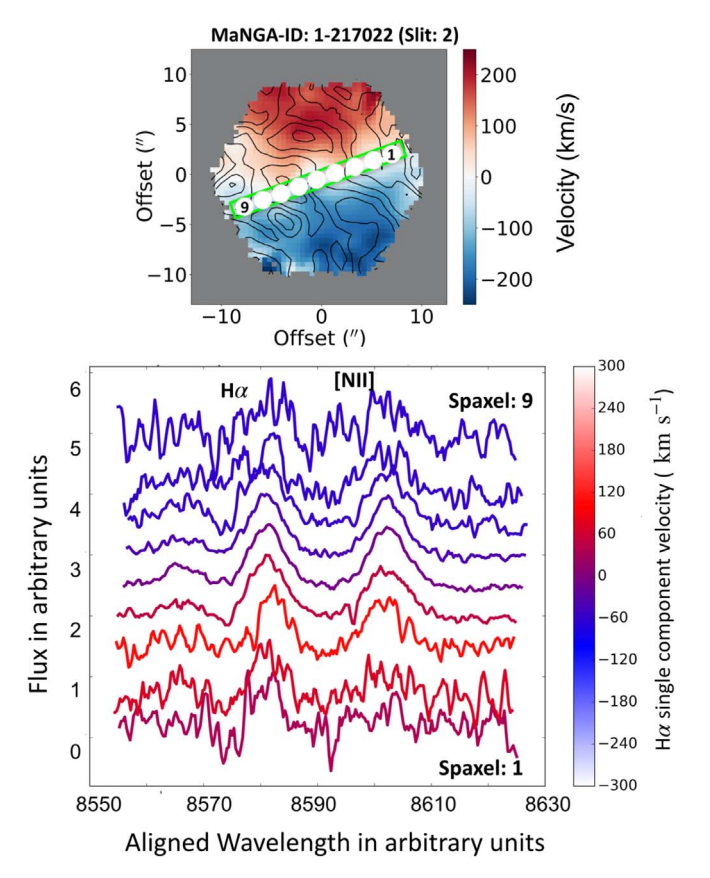


Figure 9. (Top panel) The  $H\alpha$  emission lines from the ESI for the slit 1 position of the first target galaxy are shown for different spaxels along the slit in different panels. A single or double Gaussian model, as favored by the BIC, is used to model the emission lines. For a single-component model, the model is shown in blue. For two-component models, the primary component is shown in red and the secondary in green. The modeled line profile in blue shows the total model fit to the data (which is in black). (Bottom panel) The [N II]  $\lambda$ 6584 emission line profiles in black with their model fits overplotted in blue, similar to the panel above.

with  $H\alpha$  (emission line on the left side) and [N II]  $\lambda$ 6584 (on the right) lines shown for each 1" spaxel of physical size of 0.51 kpc along the slit. The spectra are color-coded by the velocity estimate obtained by fitting the single Gaussian model to the  $H\alpha$  emission line. The spectra are then shifted along the wavelength axis so that the emission lines from the different spaxels are roughly aligned. This is done to enable easy visual comparison of the shapes and asymmetry of the emission lines.

The gas velocity amplitude rises steeply from the center outward on both the red- and blueshifted sides. The details in the emission line profiles are shown in Figure 9 via Gaussian model fits of  ${\rm H}\alpha$  and [N II] lines at different spaxels (spaxel number shown in the top right corner of each subplot). The primary velocity component reflects the bulk velocity of the ionized gas. If the double Gaussian model is preferred (according to the BIC criterion, as mentioned in Section 3.2), the line profile is asymmetric, and wings or any departures from the bulk velocity are then reflected in the secondary velocity component. The best-fit parameters for all spaxels are given in Appendix A.2.

We find that the primary velocity component (shown in red for the two-component model and blue for the one-component model; Figure 9) goes from a blueshift of  $\sim\!-250~{\rm km\,s}^{-1}$  from one end of the slit to a redshift of  $\sim\!250~{\rm km\,s}^{-1}$  at the other, closely matching the values observed from the MaNGA velocity map (Figure 8, top panel). The secondary fainter component (in green) varies widely in FWHM (2.355  $\cdot$   $\sigma$ ), ranging from  $\sim 150$  to  $600~{\rm km\,s}^{-1}$ , with broad wings near the center and the redshifted side of the galaxy. On average, emission lines with a blueshifted primary velocity component



**Figure 10.** (Top panel) MaNGA ionized gas velocity field with  $H\alpha$  EW contours overplotted in black, similar to Figure 8. The second slit position with different spaxels ( $\sim$ 1") is overlaid. (Bottom panel) The different rows indicate the observed spectra from the Keck ESI around the spectral window of  $H\alpha$  and [N II]  $\lambda$ 6584 extracted from different spaxels, as marked in the top panel. The spectra are registered to the same wavelength and color-coded by gas velocity.

show a secondary component shifted redward. The secondary component switches to the bluer side when the primary velocity component is redshifted. In other words we see a "red" wing on the blue side of the galaxy and a "blue" wing on the red side. In fact, for this particular slit position, the secondary component in certain spaxels has shifted so much relative to the primary that its velocity relative to the systemic velocity has the opposite sign compared to the primary component. That means that on the redshifted side, the blue wing is actually blueshifted relative to the systemic velocity of the galaxy, and vice versa on the other side of the galaxy. The line profiles show mostly symmetric profiles near the galaxy center where a single Gaussian model is preferred. The implications of these findings are discussed in Section 5.

For the second slit configuration (Figure 10), the slit lies almost perpendicular to the bisymmetric feature at an angle of  $110^{\circ}$  from north to east. From the  $H\alpha$  EW 2D map, it is clear that the EW of the ionized emission is enhanced along the bisymmetric feature; hence, there is comparatively less signal perpendicular to it. The spectra extracted in different spaxels along the second slit are shown in the bottom panel of Figure 10. Near the edges of the slit, line fitting becomes unsuccessful owing to low S/N. The bulk velocity in slit 2 varies from  $\sim$ 50 to  $\sim$ -50 km s<sup>-1</sup> (Figure 11). The emission lines along this slit are substantially broad, with FWHM > 250 km s<sup>-1</sup> going up to  $\sim$ 600 km s<sup>-1</sup>, similar to a few cases in slit 1. The average FWHM of the [N II] lines is higher than that

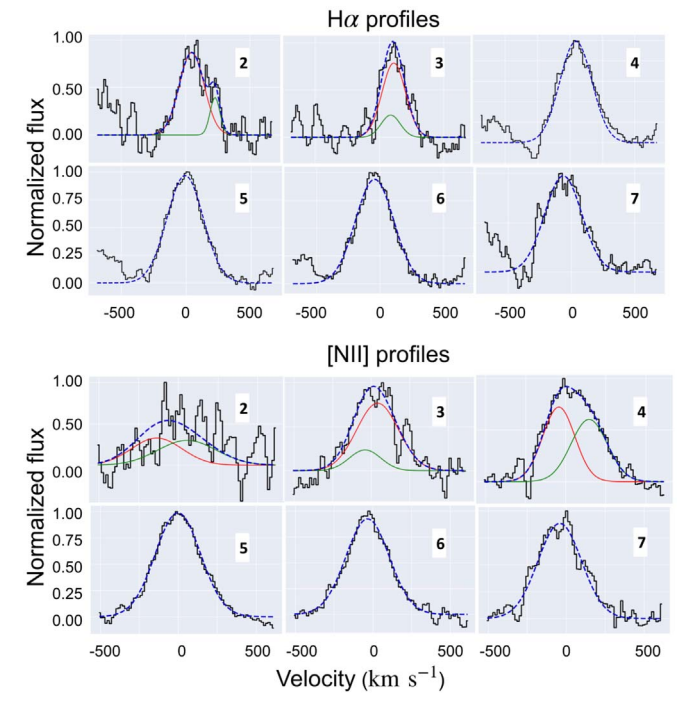


**Figure 11.** (Top panel) The  $H\alpha$  emission lines from the ESI for the slit 2 position of the first target galaxy are shown for different spaxels along the slit in different panels. A one- or two-component Gaussian model is used to model the emission lines, similar to Figure 9. The modeled line profile in blue shows the total model fit to the data (in black). (Bottom panel) Model fit for  $[N\ II]$   $\lambda 6584$  emission line profiles, similar to the subpanel above.

of the  $\text{H}\alpha$ , and broad lines (with FWHM > 300 km s<sup>-1</sup>) are observed reaching a distance of  $\sim$ 1 kpc from the center along the slit. The observed emission lines are generally symmetric across slit 2. Very slight asymmetry occasionally arises near the edges.

The third slit (Figure 12) is placed parallel to the first slit, i.e., parallel to the bisymmetric feature, but slightly off-center at a distance of  $\sim$ 2.5 kpc in the southeast direction. Owing to the decrease of ionized emission in the outskirts of the galaxy, the S/N of the spectra drops overall compared to the first slit. Nevertheless, the line profile clearly shows a red wing on the blue side of the galaxy and a blue wing on the red side, similar to slit 1 (Figure 13). The degree of asymmetry is less, but the primary velocity component goes from a blueshift of  $\sim$  200 km s<sup>-1</sup> on one end of the slit to a redshift of  $\sim$ 250 km s<sup>-1</sup> on the other. Just like slit 1, there is a significant velocity offset ( $\sim$ 100–150 km s<sup>-1</sup>) between the primary and secondary components. We note that in the MaNGA H $\alpha$  EW contour map, there is an additional H $\alpha$ -enhanced region  $\sim$ 2.9 kpc southeast of the center. The overlapping ESI spectra in the third row from the bottom (Figure 12, bottom panel) show broader H $\alpha$  and [N II] lines, possibly due to a distinct velocity component associated with this region.

#### 4.2. Target 1-145922

The second target has only one slit observation (Figure 14) with sufficient S/N spectra (a minimum S/N > 1 across the slit). The slit is oriented along the bisymmetric feature at a position angle of 320° from north to east. Despite the lower S/N, the fitting procedure was successful in extracting individual velocity components (Figure 15). The bulk velocity varies from  $\sim$  250 to  $\sim$ 300 km s<sup>-1</sup>. The average FWHM is lower

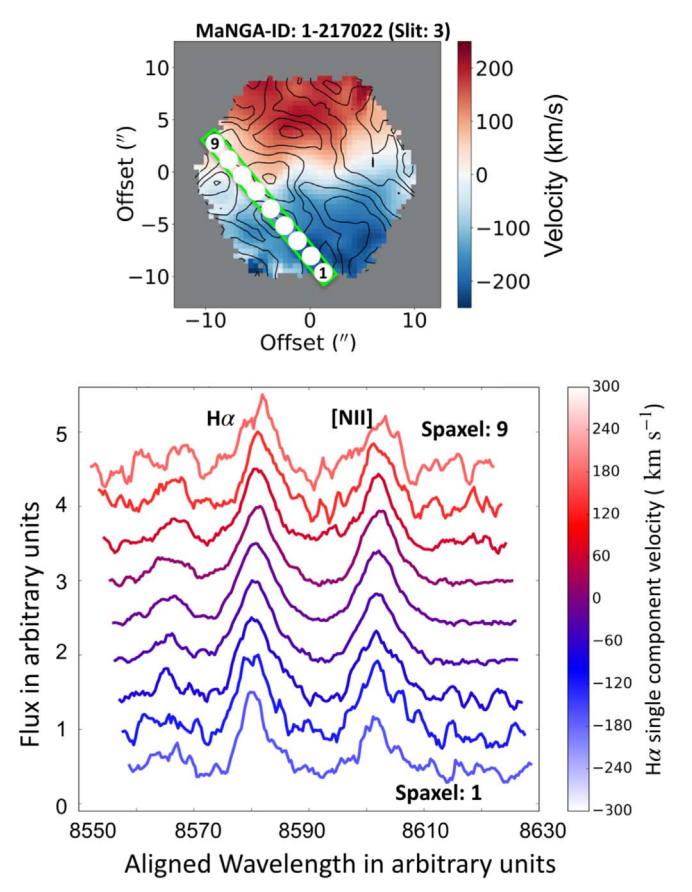


**Figure 12.** (Top panel) MaNGA ionized gas velocity field with  $H\alpha$  EW contours overplotted in black, similar to Figures 8 and 10, for the third slit position. This slit is parallel to but offset from the bisymmetric feature; hence, it traces the edge of the putative wind cone. (Bottom panel) The different rows indicate the observed  $H\alpha$  and [N II]  $\lambda$ 6584 emission lines from the Keck ESI extracted from the spaxels marked in the top panel. The spectra are registered to the same wavelength and color-coded by gas velocity.

compared to the first target, with an average value between  $\sim\!150$  and  $200\,{\rm km\,s^{-1}}$ , but it reaches a maximum value of over  $\sim\!600\,{\rm km\,s^{-1}}$  near the center. The blueshifted part of the galaxy exhibits a secondary component with a velocity  $\sim\!150\text{--}200\,{\rm km\,s^{-1}}$  redder than the primary velocity. This component provides an obvious "red" wing on the blue side. The profiles become symmetric toward the center before showing a blue wing on the redshifted side.

### 4.3. Measured Velocity Asymmetries

In order to measure the observed asymmetry of the emission lines, we fit the emission lines with a Gauss-Hermite polynomial of the form

$$f(x) = Ae^{\frac{-g^2}{2}} \left[ 1 + h_3(-\sqrt{3}g + \frac{2}{\sqrt{3}}g^3) + h_4(\frac{\sqrt{6}}{4} - \sqrt{6}g^2 + \frac{\sqrt{6}}{3}g^4) \right],$$
 (2)

where  $g = \frac{x - x_c}{\sigma}$ . Here A is the flux,  $x_c$  is the peak wavelength, and  $\sigma$  is the velocity dispersion. Departures from symmetry are quantified by the coefficient  $h_3$ , which is a proxy for the skewness parameter (k). A positive k parameter indicates the presence of a "red" wing. Similarly, blue-winged components

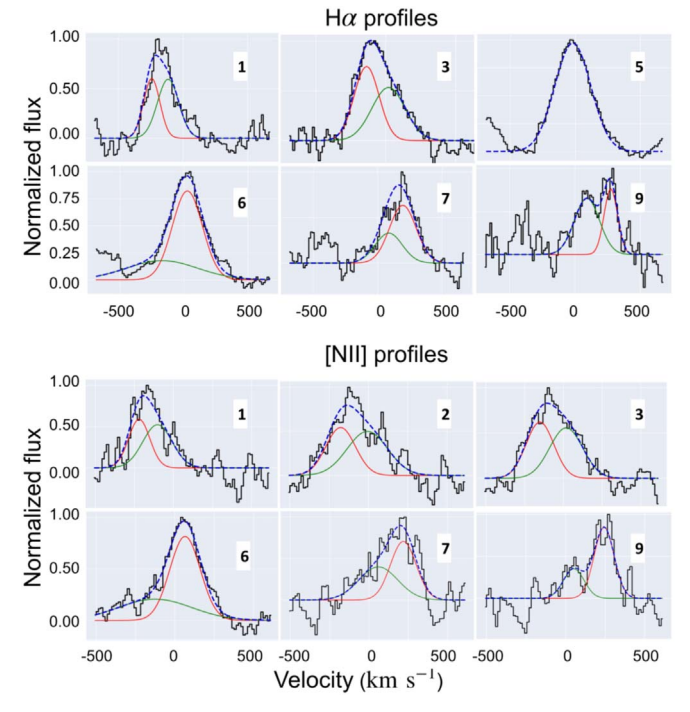


**Figure 13.** (Top panel) The  $H\alpha$  emission lines from the ESI for the slit 3 position of the first target galaxy are shown for different spaxels along the slit in different panels. A one- or two-component Gaussian model is used to model the emission lines, similar to Figure 9. The modeled line profile in blue shows the total model fit to the data (in black). (Bottom panel) Model fit for the [N II]  $\lambda 6584$  emission line profiles, similar to the panel above.

have a negative k value. Here k=0 signifies a perfectly symmetric profile. To estimate the errors on the measured skewness, we perform MCMC simulations of the above model fit for every spaxel. We construct 100 realizations of each spectrum by adding Gaussian noise with amplitude comparable to the noise measured in the original spectrum and quote the standard deviation of the k parameter distribution, thus obtained, as the  $1-\sigma$  uncertainty on the measured skewness.

In Figure 16, the k parameters obtained from the H $\alpha$  and N II  $\lambda$ 6584 Å emission lines for all four slit observations from the two galaxies are plotted against the spaxel number, which maps to locations in the slit, as shown in Figures 8–14. We can see that, for slit 1 for the first target galaxy and the only slit for the second galaxy, which sample the bisymmetric feature in the H $\alpha$ EW map, the k parameter values clearly transition from positive to negative as we move from the blueshifted side (low spaxel number) toward the redshifted side (high spaxel number) of the galaxy. This reaffirms the finding that the line profiles show a "red" wing on the blueshifted side of the galaxy and a "blue" wing on the redshifted side. The second slit of the first galaxy shows an almost flat asymmetry parameter distribution with values oscillating close to zero. This particular slit samples the central regions of the first galaxy and reveals mostly symmetric profiles. For the third slit, the k parameter values again show a transition from positive to negative values, similar to slit 1. This slit traces the outskirts of the galaxy parallel to the bisymmetric feature.

#### 5. Discussion

The main result of our observations is the systematic asymmetry of the line profiles, i.e., a red wing on the

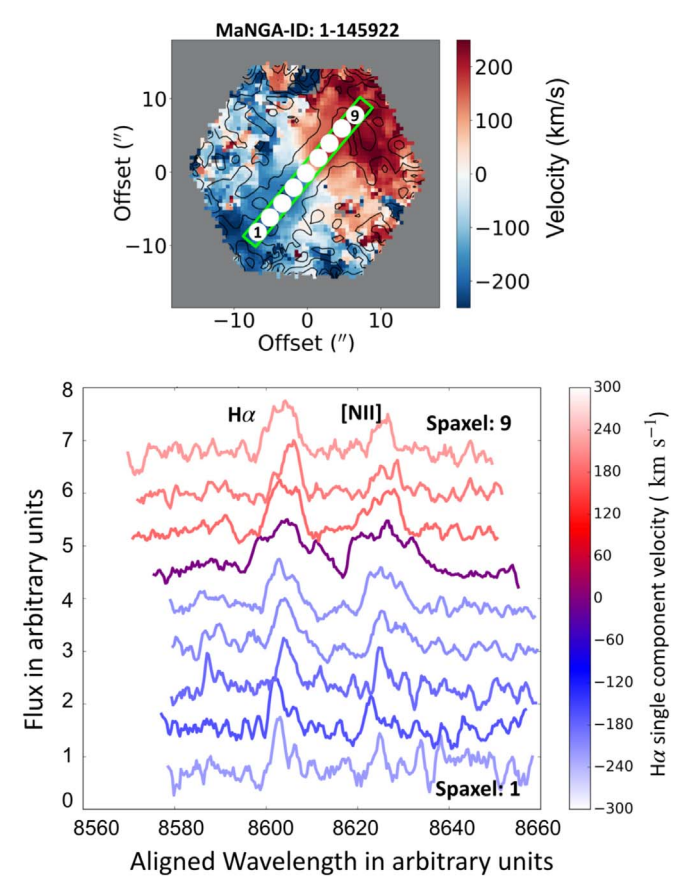


**Figure 14.** (Top panel) MaNGA ionized gas velocity field of the second target galaxy with the  $H\alpha$  EW contours overplotted in black. The only slit observation with a reasonable S/N taken for this galaxy is overlaid with different spatial bins ( $\sim$ 1") indicated with circles to map the physical location of the extracted spectra on the slit. (Bottom panel) The different rows indicate the observed ESI spectra extracted from different spaxels, as marked in the top panel. The spectra are registered to the same wavelength and color-coded by gas velocity. The spectra are generally of lower S/N compared to the first target galaxy.

blueshifted side of the galaxy and a blue wing on the redshifted side, with a symmetric profile near the center, which is observed along the bisymmetric emission feature in both of the target red geysers. Before we discuss possible interpretations in detail, we summarize our Keck ESI data using the skewness parameter k (Section 4.3) measured as a function of distance from the galaxy center along the slit (Figure 16; also shown later in Figure 20).

We will consider two physical interpretations that can give rise to our observations: ionized gas in rotation and a wideangle outflowing wind driven by an AGN.

# 5.1. Gas-in-rotation Scenario: Disk Model

In the case of a rotating disk, because the portion of the disk intersected by the line of sight is constant due to symmetry, there is no intrinsic velocity asymmetry. Instead, asymmetry profiles mainly arise from beam smearing from the point-spread function (PSF) and the spatial binning of the data, sometimes producing a similar red wing in the blueshifted side of the galaxy and vice versa, with the strength of the asymmetry roughly proportional to the velocity gradient. Beam smearing can also inflate the FWHM of the lines, especially along the regions where the projected line-of-sight velocity gradient is

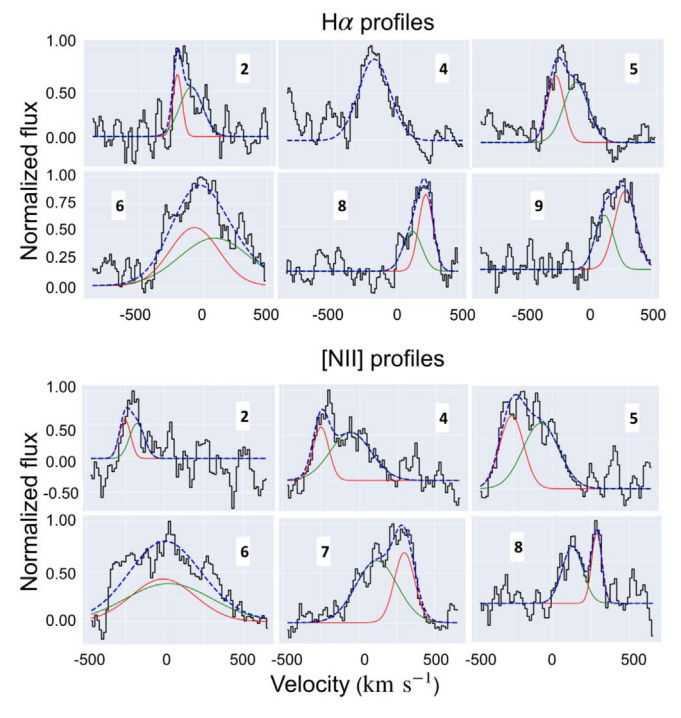


**Figure 15.** (Top panel) The  $H\alpha$  emission lines from the ESI for the only slit in the second target galaxy are shown for different spaxels along the slit in different panels. A one- or two-component Gaussian model is used to model the emission lines, similar to Figure 9. The modeled line profile in blue shows the total model fit to the data (in black). (Bottom panel) Model fit for the [N II]  $\lambda 6584$  emission line profiles, similar to the panel above.

maximum (Epinat et al. 2010; Davis et al. 2013; Green et al. 2014; Burkert et al. 2016).

Although the red geysers show multiple characteristics that argue against the disk hypothesis (see Cheung et al. 2016), it is important to address whether the Keck ESI data provide additional insight. Therefore, we construct a symmetric disk model. We use the Python version of the KINematic Molecular Simulation (KINMS) package (Davis et al. 2013)<sup>17</sup> to construct the disk model. The major advantage of using KINMS is that it self-consistently accounts for beam smearing by mocking the observations of a disk defined by the rotation curve and surface brightness profile. We assume a thin disk inclined at an angle from the observer with a velocity given by the following formula:

$$V(r, \theta) = \frac{2 V_{\text{max}}}{\pi} \tan^{-1}(r / r_{\text{turn}}).$$

Here  $V_{\text{max}}$  is the maximum velocity across the galaxy, and  $r_{\text{turn}}$  is the turnover radius for the rotation curve.

We assign an H $\alpha$  surface brightness distribution to our disk models that reproduces the MaNGA H $\alpha$  flux maps for our two galaxies, as determined by fitting an exponentially declining function of the form  $\Sigma(r) \propto e^{-\frac{r}{d_{\rm scale}}}$ , where  $d_{\rm scale}$  is the scale radius determined by the model fit. We experiment with different choices for the input parameters to find the best match between the modeled rotation curve and the position–velocity curve observed from the ESI data for both targets (see Appendix A.3). The chosen set of disk model parameters for the first galaxy are inclination = 35°, turnover radius = 9", and maximum velocity = 715 km s<sup>-1</sup>. The spatial scale and extent

of the model grid are chosen from the ESI data. For the second galaxy, the values are inclination =  $40^{\circ}$ , turnover radius = 1'', and maximum velocity =  $350 \,\mathrm{km \, s^{-1}}$ . We provide the PSF of FWHM  $\sim 0.''9$ , which roughly corresponds to the median seeing of Keck, as the "beam size" for the computation of beam smearing. We extract the projected velocity fields and line profiles at each Keck spaxel. We then calculate the asymmetry parameter (k) of the extracted line profiles in a similar way as the data (described in Section 4.3). The mock spectra extracted from the disk model along the major axis for both targets at the spatial locations of the Keck spaxels are shown in Figures 18 and 19.

We find that while the disk models can produce considerable asymmetry in the line profiles because of the beam-smearing effect, the nature of the resulting asymmetry does not match the data. For the first galaxy, the observed position-velocity curve from ESI data is almost linear, with a gentle slope (Appendix A.3, Figure 22). This causes the skewness parameter due to beam smearing of the disk (which approximately varies according to the line-of-sight velocity gradient) to rise and decline gently with less asymmetry overall compared to the data. For the second galaxy, the observed velocity curve has a sharp gradient near the center with considerable flattening at the edges (Appendix A.3, Figure 22). Hence, the skewness from the disk model is greater near the center compared to the outskirts. These findings are in accordance with other similar studies of beam smearing on star-forming disk galaxies (Green et al. 2014). Thus, the increasing asymmetry toward the outskirts of the galaxies along the kinematic axis, as observed from ESI spectra, cannot be captured by the disk model. The trend of asymmetries that we obtain from the disk model for both galaxies along the major axis of the disk are shown by (red and blue) dashed lines in Figure 20.

We see in Section 4.1 and Figure 13 that the third ESI slit, sampling locations offset from the bisymmetric feature in the first galaxy, also shows considerable asymmetry in the observed ESI spectra with a similar trend as locations along the bisymmetric feature (Figure 16). However, this level of asymmetry is not seen at similar spatial locations from the disk model, which shows a skewness value oscillating around zero. This is because the velocity gradient declines rapidly as we move parallel to the major axis of the disk away toward the outskirts. Thus, this model struggles to reproduce both the trend and the magnitude of the skewness parameter for locations offset from the kinematic major axis.

We find that the FWHM of the secondary velocity component in the observed spectra at several locations in both galaxies exceeds  $500-600 \text{ km s}^{-1}$ , a value that is quite high and typically attributed to ionized gas outflows in numerous studies (Arribas et al. 2014; Couto et al. 2017; Fischer et al. 2017; Humire et al. 2018; Soto-Pinto et al. 2019). The mock spectra extracted from the disk model for our target galaxies show an average enhancement of the velocity dispersion of about  $40-50 \,\mathrm{km \, s^{-1}}$  (or an FWHM up to  $100 \,\mathrm{km \, s^{-1}}$ ) due to beamsmearing effects, far below what we observe from data. Figures 18 and 19 (right panels) demonstrate that, apart from the central spaxel that shows the FWHM value to be much higher than average, exceeding  $\sim 150 \,\mathrm{km \, s^{-1}}$ , the modeled spectral lines from beam-smeared disks are quite narrow in the outskirts. On the other hand, the ESI spectra for both galaxies show a significantly high FWHM near the center, as well as in

<sup>17</sup> https://github.com/TimothyADavis/KinMSpy

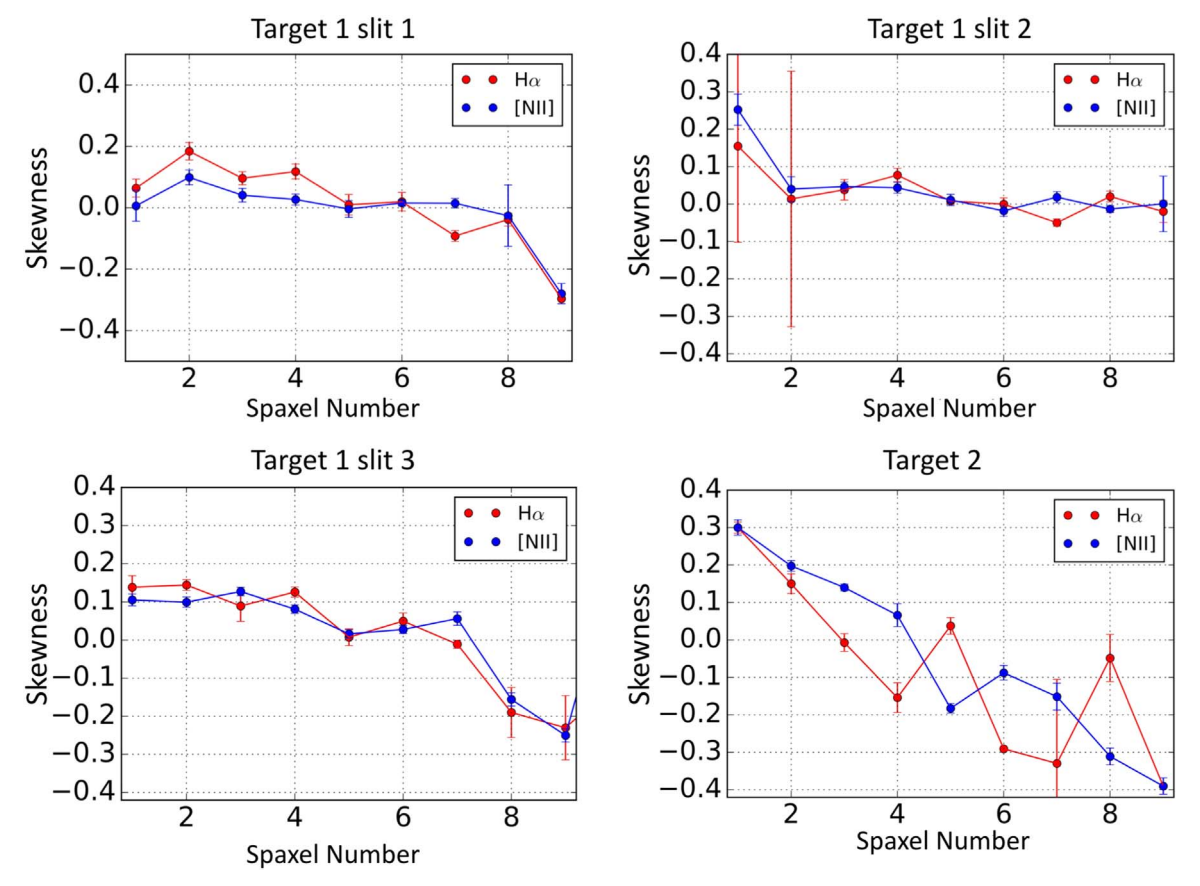


**Figure 16.** Observed Gauss–Hermite skewness of the H $\alpha$  (red) and [N II] (blue) lines for each slit position of the two target galaxies. The skewness, or the asymmetry parameter k, described in Section 4.3, quantifies the asymmetric nature of the line profiles. Here k > 0 indicates a red wing, and k < 0 indicates a blue wing. The spaxel number maps to the spatial locations in the slit, as indicated in Figures 8–14. A low spaxel number indicates the blueshifted part of the galaxy, while a high spaxel number indicates the redshifted side.

the outskirts, of the galaxies in locations along, offset from, or perpendicular to the bisymmetric feature. In other words, the enhanced dispersion does not necessarily follow the velocity field gradient, which implies that the beam-smearing effect is not the primary reason behind the observed broad lines.

#### 5.2. Outflowing Gas Scenario: Wind Model

Let us now consider the scenario of the radially outflowing motion of gas particles in a filled bicone geometry. We use a simple wind model to test our interpretation of the ESI emission line velocity profiles. A 3D Cartesian grid of points is populated with tracer particles with a uniform density that are weighted by a Hernquist profile (Hernquist 1990). The outflowing wind is assumed to be a filled wide-angle bicone centered on the galaxy. Each gas particle in the bicone is given a constant radially outward velocity directed away from the center. Those outside the bicone are given zero velocity and weight. The model is motivated by our observation that the dominant ionization in the red geysers is extended LI(N)ERlike (Figures 4 and 5) and hence the assumption that the strong emission lines (e.g.,  $H\alpha$ , [N II]) are ionized mainly by the radiation field of evolved post-asymptotic giant branch stars present around it (Yan & Blanton 2012; Belfiore et al. 2016). Although shocks can also contribute to the ionization, the smooth components of the H $\alpha$  flux distribution in red geysers typically fall off roughly proportional to the stellar surface brightness, supporting a stellar origin for the observed LINER ionization. Moreover, the exact nature of the ionization source

should not impact the model-predicted velocity profiles to first order, as both models are constrained by the observed  ${\rm H}\alpha$  flux distribution. The warm ionized gas clouds entrained by the wind trace the observed kinematics and emit emission line flux due to the assumed ionization. Hence, the projected velocity field is a convolution of the wind geometry along the line of sight and the galaxy's 3D luminosity profile. The projected line-of-sight component of the wind velocity at each point inside the bicone is weighted by its Hernquist profile value. In order to construct the luminosity distribution that gives rise to the widespread ionization of the observed gas, imaging and dynamical constraints on the stellar component obtained from Jeans anisotropic modeling (JAM; Cappellari 2008) are used for both target galaxies in the model. We use JAM analyses to find the intrinsic (3D) axis ratio and inclination of the galaxy, while the projected major-axis effective radius and sky position angle are obtained from the NSA catalog. For target 1-217022, we have taken the axis ratio to be 0.4, the galaxy inclination as 50°, the projected major-axis effective radius to be 7", and the on-sky position angle as 53° (see Cheung et al. 2016). For the second galaxy (target 1-145922), the intrinsic axis ratio is taken to be 0.5, the inclination as 20°, the projected major-axis effective radius to be 9'', and the on-sky position angle as  $-73^{\circ}$ . A detailed description of the JAM parameters for the second galaxy is presented in Appendix A.1. The wind parameters, like the opening angle, length, intrinsic velocity, and inclination of the wind cone, are varied manually until the best qualitative match is obtained between the modeled and the observed

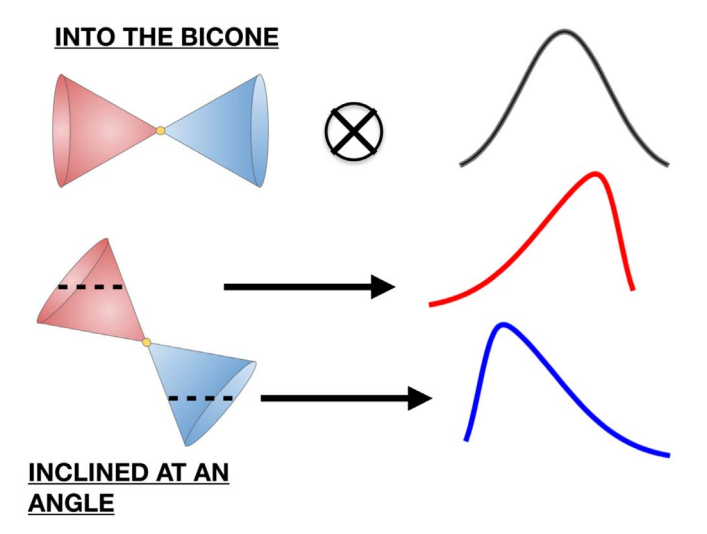


**Figure 17.** Schematic diagram showing how emission line profiles integrated along the line of sight of a conical wind are expected to produce asymmetric lines with a "blue" wing on the red side and vice versa. This behavior is evident in the emission line profiles from Keck ESI data.

MaNGA 2D gas kinematics. For the first target galaxy, the best match is found for a wind opening angle =  $80^{\circ}$ , inclination =  $75^{\circ}$ , position angle =  $55^{\circ}$ , and velocity =  $300 \, \text{km s}^{-1}$ . For the second galaxy, the wind parameters are opening angle =  $40^{\circ}$ , inclination =  $-55^{\circ}$ , PA =  $135^{\circ}$ , and velocity =  $200 \, \text{km s}^{-1}$ .

We construct a data cube consisting of spatial and spectral dimensions from the model. We assign single Gaussian emission line profiles to model gas particles throughout the 3D volume of the cone and convolve the flux distribution with a Gaussian of FWHM = 0.99 along each spatial dimension to capture the effect of beam smearing on the simulated data cube. The velocity dispersion is taken to be the instrumental dispersion ( $16 \text{ km s}^{-1}$ ). Finally, we construct spatial bins following the same slit orientation as the Keck ESI data and integrate the line profiles along lines of sight to produce mock spectra that can be compared to the ESI data.

Due to the radially outward velocity of the gas particles inside the cone, material with the greatest line-of-sight velocity component contributes the most in observed velocity and flux. Since the velocity components are integrated along the line of sight, this leads to a series of fainter components with velocities changing slightly in a systematic manner, and they add up to give a "winged" emission line profile near the two ends of the cone (Figure 17).

Moving closer to the center of the galaxy, the volume inside the cone decreases. This leads to less gas to integrate along the line of sight. The velocity variation is also comparatively less because of a much tighter configuration, and there is less variation in the angle of the velocity vector to the observer. Consequently, we expect a rather symmetric profile near the central part of the galaxies. Parallel to the axis of the cone and toward the outskirts of the galaxy, we trace the edge of the cone according to the wind hypothesis. Although the volume of the cone and the number of gas particles present toward the edge are smaller compared to those of the axis, similar asymmetries are expected, though of lesser extent.

We have extracted mock spectra from the simple outflowing wind model we constructed for both of our targets along the spatial positions that match the orientation of our slits and

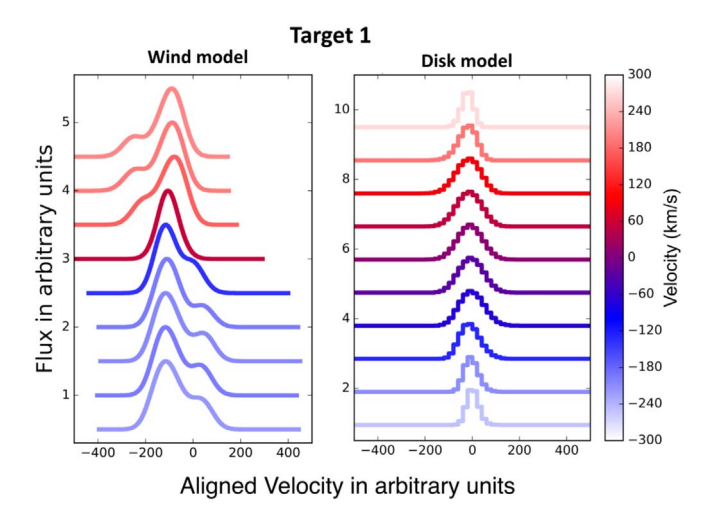


**Figure 18.** The left panel shows the mock spectra obtained from wind modeling of the first galaxy. The right panel shows the spectra obtained from the disk model. Each row in the plot represents the line-of-sight integrated spectra coadded inside each spatial bin sampling the same locations as the ESI spaxels along the bisymmetric feature in Figure 8. All of the emission lines are registered to a common velocity, and the velocity information is encoded in the color scheme.

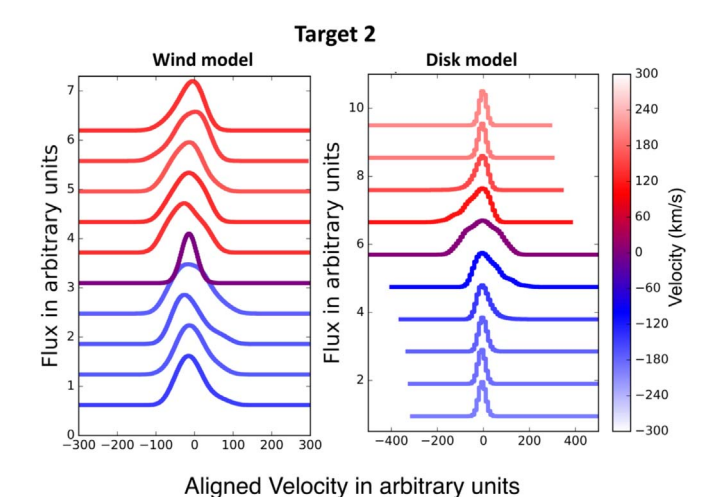


**Figure 19.** The left panel shows the mock spectra obtained from wind modeling of the second galaxy. The right panel shows that obtained from the disk model. Each row in the plot represents the line-of-sight integrated spectra coadded inside each spatial bin sampling the same locations as the ESI spaxels along the bisymmetric feature in Figure 14. All of the emission lines are registered to a common velocity, and the velocity information is encoded in the color scheme.

color-coded them by their respective observed velocity (Figures 18 and 19). The model spectra, after properly accounting for beam smearing (as we did in the disk model), have been binned spatially to match the ESI extractions. The extracted spectra in different spatial bins are plotted in different rows after being registered to a common wavelength. As in the real data, we see a clear blue wing in the redshifted side and a red wing on the blue side for the first galaxy, thus agreeing with the wind cone hypothesis for this galaxy. An additional observation from the ESI slit sampling the bisymmetric feature is that the "blue" wing on the redshifted side (and vice versa on the other side) has such a big offset from the primary component that it actually lands on the blueshifted side relative to the systematic velocity. In other words, the velocity offset between the primary and secondary components sometimes

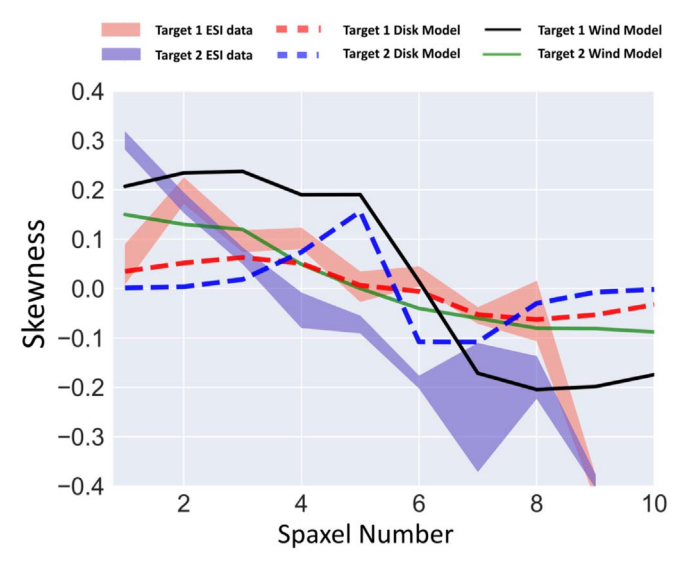


**Figure 20.** Comparison of the variation of asymmetry parameters obtained from ESI line profiles with predictions from different models. The salmon and blue shaded regions show the variation of the asymmetry parameter computed by averaging over k values from the  $H\alpha$  and [N II] lines along the presumed wind cone for both galaxies. The asymmetry parameter obtained from the disk (dashed lines) and wind (solid lines) models for the two galaxies are overplotted.

exceeds  $\sim 250 \, \mathrm{km \, s^{-1}}$ , leading the primary and secondary components to be on opposite sides of the systemic velocity. This has also been reproduced by the wind model and possibly suggests that the cone opening half-angle could be larger than the inclination, and it covers the plane of the sky.

For the wind modeling of the second galaxy, although extended wings and a systematic variation across the slit are observed, the amplitude of asymmetry is found to be weaker than the first galaxy. This might be due to the fact that the velocity field obtained from the toy wind model for the second galaxy did not fit the data as well. Further, the emission signal of the second galaxy drops considerably toward the outskirts, which makes model comparison more difficult.

We compute the asymmetry parameter k as discussed in Section 4.3 for the wind models and compare the k profiles from these simulated spectra to the ESI data and the previously discussed disk models in Figure 20. The salmon and blue shaded regions show the average asymmetry parameter variation, computed by averaging the k values of both the  $H\alpha$  and N II  $\lambda$ 6584 Å emission lines as observed from ESI data, along the bisymmetric feature for the two target galaxies. The asymmetry parameters obtained from the disk models for those two galaxies are overplotted with dashed lines, while those from the wind model are shown with solid lines. Clearly, in either target, neither the rotating disk nor the outflowing wind models fully reproduce the observed asymmetry profiles. Both models are able to reach the typical values we observe for k $(\pm 0.2-0.25)$ , but the disk models only achieve these asymmetries near the center, where beam smearing of a strong velocity gradient reaches a maximum. In the galaxy outskirts, the disk model asymmetries nearly vanish, while the observed kmagnitudes continue to increase. Both wind models reproduce this increased asymmetry in the outskirts, although they fail to match the observed magnitude of k, especially for target 2. This might be generally explained in the wind interpretation by a clumpy or turbulent outflowing medium. It is harder to explain

with a rotating disk, which requires a degree of dynamical stability in order to maintain its apparent velocity structure.

#### 6. Conclusion

We have performed an analysis of the emission line velocity profiles of H $\alpha$  and [NII]  $\lambda$ 6584 of two red geyser galaxies using high spectral resolution ( $R \sim 8000$ ) Keck ESI observations. Our observations of the first target (MaNGA ID: 1-217022) include three slit orientations that sample different parts of the galaxy, namely, the bisymmetric feature, the regions around the center, and the outskirts. The second target (MaNGA ID: 1-145922) includes only one slit observation along its bisymmetric feature. The slits that align with the biconical axis for both galaxies show strong asymmetry in the emission lines. The slit that lies parallel to the bisymmetric feature with an offset for the first galaxy also shows similar asymmetry. The shape of the emission lines, which can be decomposed into primary and secondary velocity components, exhibits a red wing on the blueshifted part of the galaxy and a blue wing on the red side, with a symmetric profile near the center. This has been quantified by an asymmetry parameter that changes systematically from positive to negative values (Figures 16 and 20). A bicone geometry of the gas with a radially outward motion can explain the observed features better than a rotating gas disk.

The presence of low-luminosity radio-mode AGNs in the red geysers (Roy et al. 2018), along with the confirmation of an outflowing wind scenario obtained from MaNGA data and the current observations from Keck ESI, lead to the evidence of AGN-driven winds in the red geyser galaxies.

This research was supported by the National Science Foundation under award No. 1816388. The authors thank the anonymous referee for helpful suggestions that significantly improved the manuscript. N.R. thanks Professor Timothy Davis for assisting with the implementation of the KINMSpy package. N.R. thanks Professor Puragra Guhathakurta and Jason Xavier Prochaska for helpful comments and discussions. S.C. acknowledges support from the Science and Technology Funding Council (STFC) via a PhD studentship (grant No. ST/ T506448/1). R.A.R. is thankful for partial financial support from the Conselho Nacional de Desenvolvimento Científico e Tecnológico (202582/2018-3 and 302280/2019-7) and Fundação de Amparo à pesquisa do Estado do Rio Grande do Sul (17/2551-0001144-9 and 16/2551-0000251-7). The authors also wish to acknowledge the very significant cultural role and reverence that the summit of Maunakea has always had within the indigenous Hawaiian community. We are very fortunate to have the opportunity to conduct observations from this mountain. Funding for the Sloan Digital Sky Survey IV has been provided by the Alfred P. Sloan Foundation, the U.S. Department of Energy Office of Science, and the Participating Institutions. The SDSS-IV acknowledges support and resources from the Center for High-Performance Computing at the University of Utah. The SDSS website is www.sdss.org.

The SDSS-IV is managed by the Astrophysical Research Consortium for the Participating Institutions of the SDSS Collaboration, including the Brazilian Participation Group, the Carnegie Institution for Science, Carnegie Mellon University, the Chilean Participation Group, the French Participation Group, the Harvard-Smithsonian Center for Astrophysics, Instituto de Astrofísica de Canarias, The Johns Hopkins University, the Kavli Institute for the Physics and Mathematics

of the Universe (IPMU)/University of Tokyo, the Korean Participation Group, Lawrence Berkeley National Laboratory, Leibniz Institut für Astrophysik Potsdam (AIP), Max-Planck-Institut für Astronomie (MPIA Heidelberg), Max-Planck-Institut für Astrophysik (MPA Garching), Max-Planck-Institut für Extraterrestrische Physik (MPE), the National Astronomical Observatories of China, New Mexico State University, New York University, the University of Notre Dame, Observatário Nacional/MCTI, The Ohio State University, Pennsylvania State University, the Shanghai Astronomical Observatory, the United Kingdom Participation Group, Universidad Nacional Autónoma de México, the University of Arizona, the University of Colorado Boulder, the University of Oxford, the University of Portsmouth, the University of Utah, the University of Virginia, the University of Washington, the University of Wisconsin, Vanderbilt University, and Yale University.

# **Appendix**

#### A.1. Recovering the Inclination Using JAM

In order to construct the wind model for the second target galaxy, we recover the inclination using the JAM method, detailed in Cappellari (2008) and implemented in the jampy package. This method approximates the stellar potential from the surface brightness distribution using multi-Gaussian expansion (MGE). In this instance, our observations of the surface brightness distribution come from R-band DESI Legacy Survey imaging (Dey et al. 2019), as this survey is deeper than the SDSS. We utilize the Python implementation of the method described in Cappellari (2002), mgefit. When constructing the MGE approximation, the flattest Gaussian in the best fit is found to be overly restrictive in the JAM modeling process, as it defines the minimum inclination that can be modeled. This is inherent to the JAM method and does not reflect a physical limitation on the inclination. We minimize this restriction while retaining suitable accuracy using the method in Scott et al. (2013). Here a limit is placed on the minimum axial ratio allowed in the MGE fit, and this limit is increased until the mean absolute deviation of the fit increases by 10%. Using this method, we found the parameters that best fit the image while maximizing the inclination range available. The parameters are presented in Table 1.

We perform an MCMC simulation to find the best-fit parameters for the JAM model to match the  $v_{\rm rms}$  map from the MaNGA data. We decide that a simple JAM model neglecting dark matter is adequate for measuring the inclination, as in Cappellari et al. (2013). The free parameters that are allowed to vary are the orbital anisotropy  $\beta$ , the inclination  $\cos i$ , and the dynamical mass-to-light ratio M/L. Both  $\beta$  and M/L are assumed to be constant across the galaxy. Note that the M/L contains components from the stellar mass-to-light ratio and the presence of dark matter, and the contribution of each of these cannot be determined by this model. We use uniform priors on each of the parameters within the bounds below.

1. The  $\beta$  is allowed to vary between zero and 0.75. Restricting  $\beta > 0$  is required to break the known degeneracy between anisotropy and inclination and is observationally motivated for fast rotators (see Section 3.1.1 of Cappellari et al. 2013), as the red geyser population is found to be.

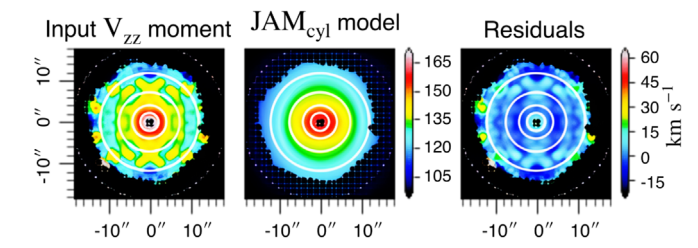


**Figure 21.** Left: symmetrized  $\nu_{rms}$  field for the galaxy that is input to JAM. Middle: output from the best-fit JAM model. Right: residuals of the model and data. The white contours in all panels trace the surface brightness of the MGE. Black dots denote masked pixels. The unit of the color bars shown is kilometers per second.

Table 1
The Parameters of the Best-fit MGE

Total Counts	σ	$q_{ m obs}$
272.886	2.47831	0.95
432.696	10.7368	0.95
165.534	21.1834	0.95
476.804	23.2103	1.0
1109.95	58.3299	1.0

**Note.** Total counts refer to the counts under each component,  $\sigma$  is the width of each component in pixels, and  $q_{\rm obs}$  is the projected axial ratio of each component.

Inclination (deg)	β	M/L
$\overline{19.58^{+0.070}_{-0.057}}$	$0.216^{+0.025}_{-0.029}$	$6.921^{+0.019}_{-0.021}$

Note. The inclination should be interpreted as an upper limit.

- 2. The  $\cos i$  is allowed to vary between zero and  $\cos i_{\min}$ , which is the minimum inclination imposed by the flattest component in the MGE approximation.
- 3. The M/L is allowed to be between zero and 10.
- 4. The  $\log f$  is an extra parameter added to quantify any underestimation of the errors and is assumed to have a uniform prior within a range between -5 and 1.

We find our best-fit model with  $\chi^2/\text{dof} = 2.68$ . The predicted  $v_{\text{rms}}$  ( $v_{zz}$ ) from the best model is shown in comparison with the observed  $v_{\text{rms}}$  in Figure 21, alongside the residuals. The measured parameters are presented in Table 2. It is noted that the best-fit inclination is close to the boundary on the prior, with artificially small errors. As such, it is believed that the true inclination may lie below the limit imposed by the MGE axial ratio

Therefore, we use an inclination of  $20^{\circ}$  to construct our wind model. The intrinsic 3D axis ratio is estimated from the inclination and the observed axis ratio from Equation (1) in Weijmans et al. (2014).

# A.2. Parameters of the Individual Velocity Components of the $H\alpha$ and [N II] Emission Lines

The best-fit parameters obtained from fitting the H $\alpha$  and [N II]  $\lambda$ 6584 Å emission lines from the ESI at different

Table 3
Best-fit Model Parameters for H $\alpha$  and [N II] Emission Lines from ESI for the Slit 1 Position of the First Target Galaxy

Spaxel	$V_1 \pm \Delta V_1  ( \mathrm{km  s}^{-1})$	$V_2 \pm \Delta V_2  (\mathrm{km}\mathrm{s}^{-1})$	$\sigma_1 \pm \Delta \sigma_1  ( \mathrm{km  s}^{-1})$	$\sigma_2 \pm \Delta \sigma_2  ( \mathrm{km  s}^{-1})$
Spaxel 1 (Hα)	$-242.99 \pm 0.54$	$-129.28 \pm 4.06$	$50.71 \pm 3.89$	$72.88 \pm 0.54$
Spaxel 1 (N II)	$-232.49 \pm 1.19$	$-129.92 \pm 5.01$	$55.02 \pm 4.92$	$59.97 \pm 1.19$
Spaxel 2 (H $\alpha$ )	$-187.46 \pm 1.59$	$-44.06 \pm 10.59$	$75.09 \pm 3.29$	$129.57 \pm 1.58$
Spaxel 2 (N II)	$-218.99 \pm 1.72$	$-48.57 \pm 1.00$	$83.84 \pm 6.84$	$131.94 \pm 1.72$
Spaxel 3 (H $\alpha$ )	$-146.59 \pm 2.96$	$-17.67 \pm 1.86$	$96.97 \pm 6$	$140.33 \pm 2.96$
Spaxel 3 (N II)	$-176.29 \pm 1.55$	$-27.29 \pm 7.10$	$87.67 \pm 6.43$	$110.11 \pm 1.55$
Spaxel 4 (H $\alpha$ )	$-132.44 \pm 2.73$	$20.27 \pm 1.23$	$84.10 \pm 2.95$	$113.93 \pm 2.73$
Spaxel 4 (N II)	$-105.67 \pm 1.27$	$4.50 \pm 14.96$	$104.90 \pm 4.83$	$143.41 \pm 1.27$
Spaxel 5(H $\alpha$ )	$-43.41 \pm 3.50$		$117.20 \pm 3.18$	•••
Spaxel 5 (N II)	$-32.20 \pm 3.10$		$132,10 \pm 2.31$	•••
Spaxel 6 (H $\alpha$ )	$-6.93 \pm 0.39$		$124.28 \pm 5.16$	•••
Spaxel 6 (N II)	$-25.25 \pm 1.76$	$13.10 \pm 5.77$	$102.63 \pm 5.23$	$164.10 \pm 1.76$
Spaxel 7 (H $\alpha$ )	$62.34 \pm 4.34$	$-126.16 \pm 13.82$	$108.73 \pm 4.93$	$276.80 \pm 4.34$
Spaxel 7 (N II)	$31.20 \pm 1.70$	$82.55 \pm 17.48$	$88.76 \pm 6.66$	$219.95 \pm 1.70$
Spaxel 8 (H $\alpha$ )	$108.87 \pm 5.49$	$92.73 \pm 3.50$	$93.15 \pm 4.87$	$278.01 \pm 5.49$
Spaxel 8 (N II)	$114.40 \pm 7.42$	$119.99 \pm 22.49$	$80.37 \pm 1.34$	$253.94 \pm 7.42$
Spaxel 9 (H $\alpha$ )	$140.16 \pm 3.94$	$-51.87 \pm 9.35$	$89.37 \pm 4.56$	$277.89 \pm 3.95$
Spaxel 9 (N II)	$61.46\pm8.06$	$232.90 \pm 8.42$	$79.12 \pm 5.09$	$79.78 \pm 8.06$

 Table 4

 Best-fit Model Parameters for  $H\alpha$  and [N II] Emission Lines from ESI for the Slit 2 Position of the First Target Galaxy

Spaxel	$V_1 \pm \Delta V_1  ( \mathrm{km  s^{-1}})$	$V_2 \pm \Delta V_2  (\mathrm{kms^{-1}})$	$\sigma_1 \pm \Delta \sigma_1  ( \mathrm{km \ s^{-1}})$	$\sigma_2 \pm \Delta \sigma_2  ( \mathrm{km  s^{-1}})$
Spaxel 1 (Hα)	$-173.12 \pm 1.24$	$21.84 \pm 4.17$	$34.40 \pm 4.31$	$103.68 \pm 1.24$
Spaxel 1 (N II)	$-136.19 \pm 3.80$	$54.99 \pm 8.83$	$159.15 \pm 3.59$	$184.52 \pm 3.80$
Spaxel 2 (H $\alpha$ )	$48.02 \pm 6.07$	$230.44 \pm 8.67$	$95.61 \pm 7.73$	$38.40 \pm 6.07$
Spaxel 2 (N II)	$41.76 \pm 1.88$	$-39.63 \pm 4.73$	$135.75 \pm 9.72$	$102.11 \pm 18.83$
Spaxel 3 (H $\alpha$ )	$111.79 \pm 16.51$	$92.17 \pm 7.53$	$92.12 \pm 8.44$	$79.78 \pm 1.65$
Spaxel 3 (N II)	$-42.28 \pm 9.21$	$146.24 \pm 11.89$	$100.06 \pm 7.51$	$112.64 \pm 9.21$
Spaxel 4 (H $\alpha$ )	$45.41 \pm 1.05$	•••	$123.75 \pm 4.95$	•••
Spaxel 4 (N II)	$-37.18 \pm 1.04$	$82.60 \pm 3.92$	$130.70 \pm 4.61$	$137.55 \pm 10.40$
Spaxel 5 (H $\alpha$ )	$-8.29 \pm 1.96$	•••	$1.3967 \pm 2.11$	•••
Spaxel 5 (N II)	$-1.71 \pm 0.53$	•••	$145.40 \pm 8.79$	•••
Spaxel 6 (H $\alpha$ )	$-41.84 \pm 1.65$	•••	$151.02 \pm 7.35$	•••
Spaxel 6 (N II)	$-33.84 \pm 1.50$	•••	$140.20 \pm 7.27$	•••
Spaxel 7 (H $\alpha$ )	$-64.86 \pm 8.12$	•••	$146.77 \pm 6.73$	•••
Spaxel 7 (N II)	$-41.25 \pm 4.55$	•••	$139.69 \pm 3.81$	•••
Spaxel 8 (H $\alpha$ )	$39.96 \pm 4.77$	$-151.19 \pm 9.21$	$51.80 \pm 4.09$	$271.33 \pm 4.77$
Spaxel 8 (N II)	$-137.07 \pm 4.43$	$52.81 \pm 9.85$	$1.95.55 \pm 9.33$	$115.53 \pm 4.43$
Spaxel 9 (H $\alpha$ )	$46.26 \pm 3.46$	$189.63 \pm 11.97$	$127.02 \pm 19.58$	$50.51 \pm 14.66$
Spaxel 9 (N II)	$1.18 \pm 3.80$	$-136.73 \pm 67.85$	$43.03 \pm 10.15$	$263.34 \pm 3.80$

slit positions for both targets are shown in Tables 3–6. The different rows in each table indicate different Keck spaxels (or spatial locations) along each slit position. If the double Gaussian model is preferred for an emission line in a particular spaxel,  $V_1$  and  $V_2$  give the primary and secondary

velocity components, while  $\sigma_1$  and  $\sigma_2$  are the corresponding dispersions. If the single-component model is preferred, the velocities and dispersions are quoted as  $V_1$  and  $\sigma_1$ , respectively, while keeping the other two columns empty.

Table 5
Best-fit Model Parameters for H $\alpha$  and [N II] Emission Lines from ESI for the Slit 3 Position of the First Target Galaxy

Spaxel	$V_1 \pm \Delta V_1  (\mathrm{kms}^{-1})$	$V_2 \pm \Delta V_2  (\mathrm{km\ s}^{-1})$	$\sigma_1 \pm \Delta \sigma_1  ( \mathrm{km  s}^{-1})$	$\sigma_2 \pm \Delta \sigma_2  ( \mathrm{km  s}^{-1})$
Spaxel 1 (Hα)	$-242.78 \pm 0.33$	$115.84 \pm 3.80$	$63.00 \pm 3.20$	$82.60 \pm 0.33$
Spaxel 1 (N II)	$-219.22 \pm 2.02$	$-100.54 \pm 10.67$	$67.73 \pm 7.41$	$94.44 \pm 2.02$
Spaxel 2 (H $\alpha$ )	$-228.87 \pm 0.59$	$-60.39 \pm 4.79$	$68.89 \pm 5.45$	$90.11 \pm 0.59$
Spaxel 2 (N II)	$176.52 \pm 1.70$	$5.75 \pm 9.39$	$93.44 \pm 5.57$	$128.30 \pm 1.71$
Spaxel 3 (H $\alpha$ )	$-136.26 \pm 5.24$	$20.39 \pm 1.59$	$89.23 \pm 3.99$	$119.42 \pm 5.24$
Spaxel 3 (N II)	$151.17 \pm 3.78$	$17.82 \pm 7.20$	$89.01 \pm 3.94$	$105.79 \pm 3.78$
Spaxel 4 (H $\alpha$ )	$-41.16 \pm 0.38$	•••	$139.24 \pm 3.26$	
Spaxel 4 (N II)	$-47.89 \pm 5.90$	$143.07 \pm 15.01$	$116.24 \pm 3.60$	$80.71 \pm 5.90$
Spaxel 5 (H $\alpha$ )	$-19.98 \pm 2.74$	•••	$138.34 \pm 2.19$	
Spaxel 5 (N II)	$-57.41 \pm 5.27$	$48.12 \pm 1.57$	$119.26 \pm 2.90$	$133.11 \pm 5.27$
Spaxel 6 (H $\alpha$ )	$26.92 \pm 1.33$	$-171.21 \pm 2.21$	$117.79 \pm 1.62$	$279.54 \pm 1.33$
Spaxel 6 (N II)	$-9.25 \pm 0.74$	$124.43 \pm 4.54$	$114.98 \pm 3.48$	$127.23 \pm 7.47$
Spaxel 7 (H $\alpha$ )	$77.83 \pm 1.80$	$117.47 \pm 5.88$	$107.12 \pm 2.29$	$279.48 \pm 1.87$
Spaxel 7 (N II)	$66.36 \pm 2.86$	$-125.50 \pm 8.55$	$97.00 \pm 2.82$	$232.33 \pm 2.86$
Spaxel 8 (H $\alpha$ )	$150.62 \pm 4.20$	$89.54 \pm 8.43$	$119.33 \pm 15.36$	$69.79 \pm 4.20$
Spaxel 8 (N II)	$90.88 \pm 17.56$	$96.00 \pm 9.07$	$113.29 \pm 9.74$	$81.11 \pm 17.56$
Spaxel 9 (H $\alpha$ )	$195.31 \pm 4.15$	$86.16 \pm 11.18$	$104.25 \pm 18.22$	$105.42 \pm 4.15$
Spaxel 9 (N II)	$217.90 \pm 11.40$	$55.42 \pm 2.74$	$81.27 \pm 6.90$	$121.58 \pm 11.40$

Spaxel	$V_1 \pm \Delta V_1  (\mathrm{km}\mathrm{s}^{-1})$	$V_2 \pm \Delta V_2  (\mathrm{km}\mathrm{s}^{-1})$	$\sigma_1 \pm \Delta \sigma_1  ( \mathrm{km  s^{-1}})$	$\sigma_2 \pm \Delta \sigma_2  ( \mathrm{km  s^{-1}})$
Spaxel 1 (Hα)	$-2.7671 \pm 1.14$	$-2.0153 \pm 5.28$	$3.603 \pm 5.40$	$3.878 \pm 1.14$
Spaxel 1 (N II)	$238.34 \pm 1.33$	$208.225 \pm 9.18$	$44.54 \pm 1.05$	$74.47 \pm 1.35$
Spaxel 2 (H $\alpha$ )	$-220.52 \pm 1.72$	$-113.65 \pm 15.92$	$34.95 \pm 4.19$	$90.50 \pm 1.72$
Spaxel 2 (N II)	$-242.04 \pm 5.73$	$-170.61 \pm 10.42$	$48.34 \pm 1.53$	$38.85 \pm 5.73$
Spaxel 3 (H $\alpha$ )	$-248.59 \pm 1.50$	$-140.43 \pm 7.74$	$66.76 \pm 15.01$	$69.92 \pm 1.50$
Spaxel 3 (N II)	$-252.36 \pm 1.98$	$-175.73 \pm 12.18$	$35.82 \pm 5.18$	$47.31 \pm 1.98$
Spaxel 4 (H $\alpha$ )	$-278.44 \pm 3.16$	$-196.77 \pm 6.57$	$200.93 \pm 4.51$	$73.13 \pm 3.16$
Spaxel 4 (N II)	$-267.96 \pm 4.07$	$-176.50 \pm 2.13$	$82.67 \pm 4.51$	$58.05 \pm 1.64$
Spaxel 5 (H $\alpha$ )	$-291.78 \pm 2.10$	•••	$122.62 \pm 4.62$	•••
Spaxel 5 (N II)	$-251.27 \pm 0.98$	$-58.79 \pm 6.48$	$5.085 \pm 4.07$	$1.3221 \pm 0.98$
Spaxel 6 (H $\alpha$ )	$-73.24 \pm 4.35$	$88.08 \pm 2.37$	$193.27 \pm 8.75$	$276.89 \pm 4.35$
Spaxel 6 (N II)	$-263.89 \pm 9.87$	$-73.19 \pm 1.17$	$78.04 \pm 8.41$	$118.16 \pm 9.87$
Spaxel 7 (H $\alpha$ )	$132.66 \pm 7.47$	$313.36 \pm 5.72$	$93.72 \pm 6.07$	$46.42 \pm 7.47$
Spaxel 7 (N II)	$-14.07 \pm 1.67$	$22.35 \pm 3.09$	$202.62 \pm 2.47$	$274.48 \pm 16.43$
Spaxel 8 (H $\alpha$ )	$228.31 \pm 14.59$	$120.40 \pm 5.19$	$57.39 \pm 1.03$	$73.28 \pm 1.45$
Spaxel 8 (N II)	$300.75 \pm 6.15$	$117.76 \pm 10.83$	$66.50 \pm 6.06$	$136.84 \pm 6.15$
Spaxel 9 (H $\alpha$ )	$277.58 \pm 19.22$	$113.62 \pm 2.13$	$84.19 \pm 1.35$	$72.06 \pm 1.92$
Spaxel 9 (N II)	$287.129 \pm 4.40$	$130.03 \pm 8.94$	$32.69 \pm 2.67$	$66.05 \pm 4.40$

# A.3. Rotation Curves and Spatially Resolved Velocity Maps from the Disk Model

Using the KINMSpy package, we construct a thin disk model defined by turnover radius, thickness of the disk, maximum velocity attained by the rotation curve, and scale radius associated with the assumed surface brightness profile for each of our target galaxies. The set of parameters chosen to best represent the observed target galaxies (see Section 5 for details) are decided based on the qualitative match between the modeled rotation curve and the observed velocity

curve from ESI. The comparison between the ESI data (magenta circles) and those obtained from the model (yellow contours) is shown in Figure 22. The fair match between the rotation curves confirms the best possible choice of the disk parameters in an attempt to reproduce the data. Figure 23 shows the corresponding 2D spatially resolved velocity map of the modeled gas particles obtained from the thin disk model using the chosen set of parameters. The observed 2D velocity fields are harder to reproduce using the disk model for both galaxies.

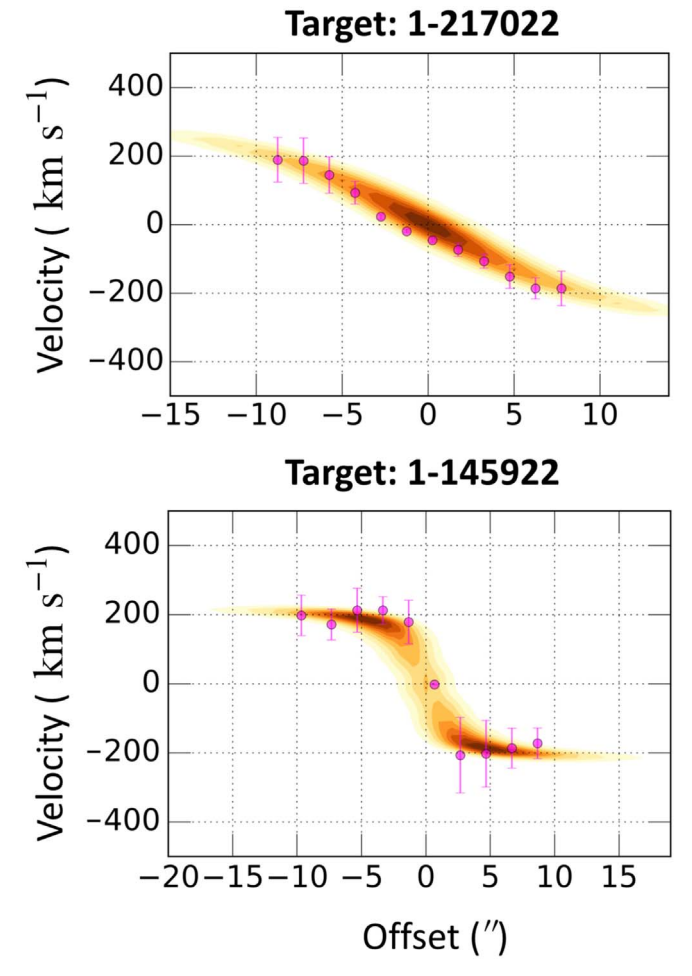


**Figure 22.** Position–velocity curve from the ESI data (magenta circles) overplotted on the best-matched rotation curve, assuming a disk model (details in Section 5; yellow contours) for both target galaxies. The parameters of the disk model are chosen based on this qualitative match.

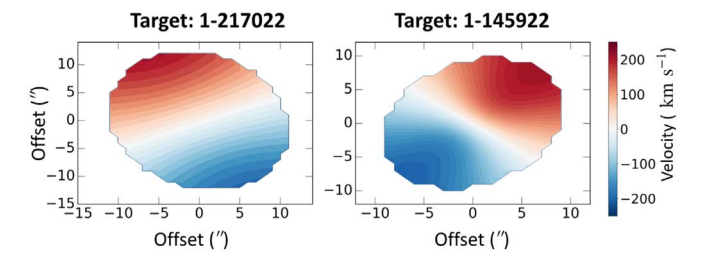


**Figure 23.** Spatially resolved 2D gas velocity map obtained from the best-matched disk model for the first (left panel) and second (right panel) target galaxies.

### **ORCID iDs**

Namrata Roy https://orcid.org/0000-0002-4430-8846 Kevin Bundy https://orcid.org/0000-0001-9742-3138 Francesco Belfiore https://orcid.org/0000-0002-2545-5752 Renbin Yan https://orcid.org/0000-0003-1025-1711 Rogemar A. Riffel https://orcid.org/0000-0003-0483-3723 Matthew Bershady https://orcid.org/0000-0002-3131-4374 Kyle Westfall https://orcid.org/0000-0003-1809-6920 Niv Drory https://orcid.org/0000-0002-7339-3170 Kai Zhang https://orcid.org/0000-0002-9808-3646

#### References

```
Albareti, F. D., Prieto, C. A., Almeida, A., et al. 2017, ApJS, 233, 25
Arribas, S., Colina, L., Bellocchi, E., et al. 2014, A&A, 568, A14
Baldwin, J. A., Phillips, M. M., & Terlevich, R. 1981, PASP, 93, 5
Belfiore, F., Maiolino, R., Maraston, C., et al. 2016, MNRAS, 461, 3111
Belfiore, F., Westfall, K. B., Schaefer, A., et al. 2019, AJ, 158, 160
Bell, E. F., Wolf, C., Meisenheimer, K., et al. 2004, ApJ, 608, 752
Binney, J., & Tabor, G. 1995, MNRAS, 276, 663
Blanton, M. R., Bershady, M. A., Abolfathi, B., et al. 2017, AJ, 154, 28
Blanton, M. R., Kazin, E., Muna, D., et al. 2011, AJ, 142, 31
Blanton, M. R., & Roweis, S. 2007, AJ, 133, 734
Bower, R. G., Benson, A. J., Malbon, R., et al. 2006, MNRAS, 370, 645
Bryant, J. J., Croom, S. M., van de Sande, J., et al. 2019, MNRAS, 483, 458
Bundy, K., Bershady, M. A., Law, D. R., et al. 2015, ApJ, 798, 7
Bundy, K., Ellis, R. S., Conselice, C. J., et al. 2006, ApJ, 651, 120
Burkert, A., Förster Schreiber, N. M., Genzel, R., et al. 2016, ApJ, 826, 214
Cappellari, M. 2002, MNRAS, 333, 400
Cappellari, M. 2008, MNRAS, 390, 71
Cappellari, M. 2017, MNRAS, 466, 798
Cappellari, M., & Emsellem, E. 2004, PASP, 116, 138
Cappellari, M., Scott, N., Alatalo, K., et al. 2013, MNRAS, 432, 1709
Cattaneo, A., Faber, S. M., Binney, J., et al. 2009, Natur, 460, 213
Chang, Y.-Y., van der Wel, A., da Cunha, E., & Rix, H.-W. 2015, ApJS, 219, 8
Chen, Y.-M., Shi, Y., Tremonti, C. A., et al. 2016, NatCo, 7, 13269
Cheung, E., Bundy, K., Cappellari, M., et al. 2016, Natur, 533, 504
Ciotti, L., & Ostriker, J. P. 2001, ApJ, 551, 131
Ciotti, L., & Ostriker, J. P. 2007, ApJ, 665, 1038
Ciotti, L., Ostriker, J. P., & Proga, D. 2010, ApJ, 717, 708
Couto, G. S., Storchi-Bergmann, T., & Schnorr-Müller, A. 2017, MNRAS,
Croton, D. J., Springel, V., White, S. D. M., et al. 2006, MNRAS, 365, 11
Davis, T. A., Alatalo, K., Bureau, M., et al. 2013, MNRAS, 429, 534
Davis, T. A., & Bureau, M. 2016, MNRAS, 457, 272
Dey, A., Schlegel, D. J., Lang, D., et al. 2019, AJ, 157, 168
Drory, N., MacDonald, N., Bershady, M. A., et al. 2015, AJ, 149, 77
Duckworth, C., Starkenburg, T. K., Genel, S., et al. 2020, MNRAS, 495, 4542
Dunn, R. J. H., & Fabian, A. C. 2006, MNRAS, 373, 959
Epinat, B., Amram, P., Balkowski, C., et al. 2010, MNRAS, 401, 2113
Faber, S. M., Willmer, C. N. A., Wolf, C., et al. 2007, ApJ, 665, 265
Fabian, A. C. 1994, ARA&A, 32, 277
Fabian, A. C. 2012, ARA&A, 50, 455
Fabian, A. C., Sanders, J. S., Taylor, G. B., et al. 2006, MNRAS, 366, 417
Falcón-Barroso, J., Sánchez-Blázquez, P., Vazdekis, A., et al. 2011, A&A,
Fischer, T. C., Machuca, C., Diniz, M. R., et al. 2017, ApJ, 834, 30
Gomes, J. M., Papaderos, P., Kehrig, C., et al. 2016, A&A, 588, A68
Graham, M. T., Cappellari, M., Li, H., et al. 2018, MNRAS, 477, 4711
Green, A. W., Glazebrook, K., McGregor, P. J., et al. 2014, MNRAS,
  437, 1070
Gunn, J. E., Siegmund, W. A., Mannery, E. J., et al. 2006, AJ, 131, 2332
Heckman, T. M., & Best, P. N. 2014, ARA&A, 52, 589
Hernquist, L. 1990, ApJ, 356, 359
Higson, E., Handley, W., Hobson, M., et al. 2019, Stat. Comput., 29, 891
Humire, P. K., Nagar, N. M., Finlez, C., et al. 2018, A&A, 614, A94
Ilbert, O., Salvato, M., Le Floc'h, E., et al. 2010, ApJ, 709, 644
Lagos, C. del P., Davis, T. A., Lacey, C. G., et al. 2014, MNRAS, 443,
Lagos, C. P., Crain, R. A., & Schaye, J. 2015, MNRAS, 452, 3815
Law, D. R., Cherinka, B., Yan, R., et al. 2016, AJ, 152, 83
Law, D. R., Westfall, K. B., Bershady, M. A., et al. 2021, AJ, 161, 52
Law, D. R., Yan, R., Bershady, M. A., et al. 2015, AJ, 150, 19
Martin, D. C., Fanson, J., Schiminovich, D., et al. 2005, ApJL, 619, L1
McNamara, B. R., & Nulsen, P. E. J. 2007, ARA&A, 45, 1388
Moustakas, J., Coil, A. L., Aird, J., et al. 2013, ApJ, 767, 50
Riffel, R. A., Nemmen, R. S., Ilha, G. S., et al. 2019, MNRAS, 485, 5590
Roy, N., Bundy, K., Cheung, E., Rujopakarn, W., et al. 2018, ApJ, 869,
Salim, S., Lee, J. C., Janowiecki, S., et al. 2016, ApJS, 227, 2
Sarzi, M., Falcón-Barroso, J., Davies, R. L., et al. 2006, MNRAS, 366, 1151
Scott, N., Cappellari, M., Davies, R. L., et al. 2013, MNRAS, 432, 1894
Skilling, J. 2004, in AIP Conf. Proc. 735, Bayesian Inference and Maximum
  Entropy Methods in Science and Engineering: 24th Int. Workshop on
   Bayesian Inference and Maximum Entropy Methods in Science and
```

Engineering, ed. R. Fischer, R. Preuss, & U. von Toussaint (Melville,

NY: AIP), 395

```
Skilling, J. 2006, BayAn, 1, 833
Smee, S. A., Gunn, J. E., Uomoto, A., et al. 2013, AJ, 146, 32
Soto-Pinto, P., Nagar, N. M., Finlez, C., et al. 2019, MNRAS, 489, 4111
Speagle, J. S. 2020, MNRAS, 493, 3132
Starkenburg, T. K., Sales, L. V., Genel, S., et al. 2019, ApJ, 878, 143
van de Voort, F., Davis, T. A., Kereš, D., et al. 2015, MNRAS, 451, 3269
Wake, D. A., Bundy, K., Diamond-Stanic, A. M., et al. 2017, AJ, 154, 86
```

```
Weijmans, A.-M., de Zeeuw, P. T., Emsellem, E., et al. 2014, MNRAS, 444, 3340
Westfall, K. B., Cappellari, M., Bershady, M. A., et al. 2019, AJ, 158, 231
Yan, R., & Blanton, M. R. 2012, ApJ, 747, 61
Yan, R., Bundy, K., Law, D. R., et al. 2016a, AJ, 152, 197
Yan, R., Tremonti, C., Bershady, M. A., et al. 2016b, AJ, 151, 8
Yuan, F., & Narayan, R. 2014, ARA&A, 52, 529
```